



JGR Atmospheres



RESEARCH ARTICLE

10.1029/2023JD039425

Key Points:

- Numerical simulations of gravity waves (GWs) over Syowa Station, Antarctic, successfully reproduce their amplitudes and momentum fluxes
- Ship-wave responses along the coastal terrain and wave filtering in the vertical structure of background winds are observed
- GWs are radiated from the lift of an airmass along an isentropic surface hump associated with a near-surface a hydraulic jump

Supporting Information:

Supporting Information may be found in the online version of this article.

Correspondence to:

M. Kohma, kohmasa@eps.s.u-tokyo.ac.jp

Citation:

Kohma, M., Sato, K., Fritts, D. C., & Lund, T. S. (2024). Numerical simulation of orographic gravity waves observed over Syowa Station: Wave propagation and breaking in the troposphere and lower stratosphere. *Journal of Geophysical Research: Atmospheres*, 129, e2023JD039425. https://doi.org/10.1029/2023JD039425

Received 8 JUN 2023 Accepted 13 JAN 2024

© 2024. The Authors. This is an open access article under the terms of the Creative Commons Attribution License, which permits use, distribution and reproduction in any medium, provided the original work is properly cited.

Numerical Simulation of Orographic Gravity Waves Observed Over Syowa Station: Wave Propagation and Breaking in the Troposphere and Lower Stratosphere

M. Kohma¹, K. Sato¹, D. C. Fritts², and T. S. Lund²

¹Department of Earth and Planetary Science, Graduate School of Science, The University of Tokyo, Tokyo, Japan, ²GATS, Boulder, CO, USA

Abstract A high-resolution model in conjunction with realistic background wind and temperature profiles has been used to simulate gravity waves (GWs) that were observed by an atmospheric radar at Syowa Station, Antarctica on 18 May 2021. The simulation successfully reproduces the observed features of the GWs, including the amplitude of vertical wind disturbances in the troposphere and vertical fluxes of northward momentum in the lower stratosphere. In the troposphere, ship-wave responses are seen along the coastal topography, while in the stratosphere, critical-level filtering due to the directional shear causes significant change of the wave pattern. The simulation shows the multi-layer structure of small-scale turbulent vorticity around the critical level, where turbulent energy dissipation rates estimated from the radar spectral widths were large, indicative of GW breaking. Another interesting feature of the simulation is a wave pattern with a horizontal wavelength of about 25 km, whose phase lines are aligned with the front of turbulent wake downwind of a hydraulic jump that occurs over steep terrain near the coastline. It is suggested that the GWs are likely radiated from the adiabatic lift of an airmass along an isentropic surface hump near the ground, which explains certain features of the observed GWs in the lower stratosphere.

Plain Language Summary In this study, a high-resolution computer model was used to simulate atmospheric gravity waves (GWs) that were observed by an atmospheric radar in Antarctica. The simulation successfully reproduced the characteristics of the observed GWs, such as the strength of vertical wind disturbances observed from the ground to 8 km altitude. The simulation showed ship-wave-like responses along the Antarctic coast, while, at higher altitudes, the wave pattern changed significantly due to the vertical structure of the background wind. Another interesting finding from the simulation is the presence of a wave pattern with a horizontal wavelength of approximately 25 km. The wavefronts of these waves align with the turbulent region formed downwind of a steep terrain along the coastline. The GWs are likely generated by the uplift of air along a particular type of atmospheric feature near the ground, which explain the upward transport of momentum observed by the radar.

1. Introduction

Gravity waves (GWs) play a critical role in transporting momentum from the troposphere to higher altitudes where it is often deposited by turbulent or viscous mechanisms and driving meridional circulations in the middle atmosphere. Additionally, turbulence associated with GW breaking play a role in mixing of heat, momentum, and minor constituents (Fritts & Alexander, 2003). However, obtaining the global characteristics of GWs is challenging due to their small scales, short periods, and highly intermittent nature. GWs can arise from various sources, including flow lifting along mountains (R. B. Smith, 2019; and references therein) as well as other non-orographic processes such as convection and jet imbalance (e.g., Fovell et al., 1992; Grimsdell et al., 2010; O'Sullivan & Dunkerton, 1995; Plougonven & Snyder, 2007; Yasuda et al., 2015). Previous studies have identified GW generation near the ground, notably in association with undulations above the convective boundary layer (e.g., Kuettner et al., 1987), the leading edge of a GW current (e.g., Ralph et al., 1993), cold fronts (e.g., Plougonven & Snyder, 2007; Ralph et al., 1999), and sea surface temperature fronts (Kilpatrick et al., 2014). Such phenomena are characterized by humps of an isentropic surface, which act as atmospheric obstacles. They can induce uplift in the airflow, facilitating GW generation (Plougonven & Zhang, 2014).

In general circulation models (GCM) and numerical weather predictions, GW parameterizations are used to calculate momentum deposition due to subgrid-scale (unresolved) GWs from explicitly resolved fields. To

KOHMA ET AL. 1 of 22

21698996, 2024, 3, Downloaded from https

wiley.com/doi/10.1029/2023JD039425, Wiley Online Library on [02/12/2024]. See the Terms

are governed by the applicable Creative Commons License

increase computational efficiency, most GW parameterizations are based on several simplifications of GWs including vertical-only propagation (namely, no lateral propagation), instantaneous response at higher altitudes, and linear/slowly varying GW amplitudes (M. J. Alexander et al., 2010; Kim et al., 2003). Recent studies using ground-based, airborne, satellite observations as well as high-resolution numerical simulations, however, suggest that such simplifications are not always valid. For example, lateral propagation of GW packets over great distances is ubiquitously observed in satellite observations (e.g., Hindley et al., 2019; Wright et al., 2017) and high-resolution numerical simulations (e.g., Kruse et al., 2022; Sato et al., 2009, 2012). Several observational studies suggest secondary GW generation in the stratosphere, mesosphere, and thermosphere (e.g., Bossert et al., 2015; Dong et al., 2021; Fritts et al., 2016, 2018; S. M. Smith et al., 2013).

Lund et al. (2020) and Fritts et al. (2021) conducted high-resolution numerical simulations of mountain wave (MW) generation and responses that extended into the mesosphere and lower thermosphere (MLT). They demonstrated the nonlinear dynamics of MW over the southern Andes, including strong wave breaking in the stratosphere and mesosphere, excitation of secondary GWs and acoustic waves, and filtering and modulation of GWs in background vertical shear. Fritts et al. (2022a, 2022b) examined their model's ability to capture MW responses based on the horizontal resolution. They showed that reducing horizontal resolution from 1 to 2 km resulted in significant differences including wave breaking altitudes and strength of responses in the MLT region. Further reductions caused suppression of instability and wave-mean flow interaction, as suggested by previous studies (Fritts et al., 2018; Vosper, 2015; Vosper et al., 2016). These studies suggest that the numerical simulations with horizontal grid spacing of 1 km or less are necessary to capture realistic MW responses.

The present study focuses on a simulation of MWs observed over Syowa Station, Antarctic (69.0°S, 40.5°E) on 18 May 2021 using a high-resolution numerical model. Although there were limited number of studies of GWs in the Antarctic region due to the harsh environment, there has been a growing interest in recent years. This surge in interest is evidenced by studies employing balloon-borne observations (e.g., Hertzog et al., 2008; Jewtoukoff et al., 2015; Li et al., 2009; Murphy et al., 2014; Pfenninger et al., 1999; Sato & Yoshiki, 2008; Yoo et al., 2018), remote-sensing techniques (e.g., M. J. Alexander & Teitelbaum, 2007; Arnault & Kirkwood, 2012; Kaifler et al., 2015; Kogure et al., 2017; Yamashita et al., 2009), and numerical models (e.g., S. P. Alexander et al., 2017; Kruse et al., 2022; Sato et al., 2012; Vadas & Becker, 2018; Vignon et al., 2020). Furthermore, GWs in the Antarctic region are known to play significant roles not only in the momentum deposition in the middle atmosphere (McLandress et al., 2012; Sato et al., 2009) but also in the production and compositions of polar stratospheric clouds (S. P. Alexander et al., 2011, 2013; Kohma & Sato, 2011; Noel & Pitts, 2012; Watanabe et al., 2006). Recent studies based on observations from a Mesosphere-Stratosphere-Troposphere (MST) radar at Syowa Station provide new insights into GWs in the Antarctic region, including their momentum fluxes (Sato et al., 2014, 2017; Shibuya et al., 2017), wave parameters (Minamihara et al., 2018), and their intermittency (Minamihara et al., 2020). The estimated turbulent energy dissipation rate is also used to examine the relation between GWs and turbulence (Kohma et al., 2019, 2021; Minamihara et al., 2023). Although there have been several studies based on numerical simulations of GWs observed over Syowa Station (e.g., Minamihara et al., 2023; Shibuya et al., 2017), they are based on calculations with horizontal grid spacings of 2.8 km or larger.

Our goal in this paper is to simulate Antarctic MWs with horizontal resolution of 250 m in order to accurately depict their responses in the troposphere and stratosphere, and to compare these results with the radar observations at Syowa Station. The present paper is organized as follows: The radar observations at Syowa Station are introduced in Section 2. Model description and specification of numerical experiments are described in Section 3. In Section 4, winds and momentum fluxes associated with GWs observed on 18 May 2021 over Syowa Station are described. Turbulent energy dissipation rates estimated from radar Doppler spectral widths are also shown. Wave characteristics seen in the numerical experiments including vertical propagation with directional shear, breaking around the critical level, and momentum fluxes are described in Section 5. Section 6 discusses an interesting feature seen in the simulation, which is the wave generation from the isentropic surface hump near the ground. Finally, Section 7 provides a summary and concluding remarks.

2. Observational Data Over Syowa Station

2.1. VHF Radar Observations

The present study used observations from the Program of Antarctic Syowa MST/Incoherent Scatter radar (PANSY radar). The radar parameters are summarized in Table 1, and a detailed specification of the radar is described in

KOHMA ET AL. 2 of 22

.com/doi/10.1029/2023JD039425, Wiley Online Library on [02/12/2024]. See the Terms and Conditi

Parameters of the Program of Antarctic Syowa MST/Incoherent Scatter Radar

| Title | Value |
|-----------------------------|--|
| Location | Syowa Station, Antarctic (69.00°S, 39.35°E) |
| Operating central frequency | 47.0 MHz |
| Inter-pulse period | 320 μs |
| Peak power output | 520 kW |
| Coherent integration | 64 times |
| Incoherent integration | 7 times |
| Nyquist velocity | ±15.6 m/s |
| Spectral resolution | 0.244 m/s |
| Range resolution | 150 m |
| Number of beams | 5 (vertical + 10° oblique to N. S. E. and W.) |

Sato et al. (2014). The PANSY radar has provided near continuous observations since 30 April 2012. Since late September 2015, the system was brought to its current capabilities. The wind estimation method is described in Sato et al. (1997) and Fukao et al. (2014).

Turbulent energy dissipation rates (ε) are estimated from widths of the radar Doppler spectra following Kohma et al. (2019) and Nishimura et al. (2020). We estimated ε using measurements by four oblique (northward, eastward, southward, and westward) beams with a zenith angle of 10° in order to eliminate specular reflection that affects the spectrum for the vertical beam (e.g., Tsuda et al., 1986). For calculating the spectral widths due to turbulent wind fluctuations, non-turbulent broadening effects need to be removed. Since the two-way beam pattern was not axially symmetric due to the irregular antenna distribution of the PANSY radar, the conventional formula for beam broadening effect for a symmetric antenna distribution (Hocking, 1985) is questionable for the radar. In the present study, we extracted the turbulent velocity variance considering the antenna distribution following an algorithm developed by Nishimura et al. (2020), in which the beam broadening component is subtracted with deconvolution operation for the measured radar spectra. The

velocity variance due to turbulence in a stably stratified flow is related to $\varepsilon = c_R v'^2 N$, where v'^2 and N is velocity variance and buoyancy frequency, respectively (Hocking, 1983; Weinstock, 1981). In the present study, c_R was set to 0.45 while a value of 0.45–0.5 for c_R is typically used in previous studies (e.g., Hocking, 1999; Wilson, 2004). Temperature profiles from operational radiosonde observations are used for calculation of $N^2 = g/\theta \partial \theta/\partial z$, where θ and g are potential temperature and gravitational acceleration. The present study shows the average ε value from the four oblique beams.

2.2. Reanalysis Data

The present study used the fifth major global reanalysis produced by ECMWF (ERA5; Hersbach et al., 2020) with a $0.5^{\circ} \times 0.5^{\circ}$ regular latitude-longitude grid to calculate the height of the dynamical tropopause (Hoskins et al., 1985). Here, the dynamical tropopause height is defined as the height with a potential vorticity (PV) of -2×10^{-6} Km² kg⁻¹ s⁻¹. The PV values over Syowa Station were obtained by linear interpolation.

3. Numerical Model and Simulation Set-Up

3.1. Model and Computational Domain

For the numerical experiment, we used the Complex Geometry Compressible Atmospheric Model, which is a finite-volume code for compressible Navier-Stokes equations (Fritts et al., 2021; Lund et al., 2020). The governing equation is as follows:

$$\frac{\partial \rho}{\partial t} + \frac{\partial \rho u_j}{\partial x_j} = 0,\tag{1}$$

$$\frac{\partial \rho u_i}{\partial t} + \frac{\partial \rho u_i u_j}{\partial x_i} = -\frac{\partial p}{\partial x_i} - \rho g \delta_{i3} + \frac{\partial \sigma_{ij}}{\partial x_i},\tag{2}$$

$$\frac{\partial \rho E}{\partial t} + \frac{\partial (\rho E + p)u_j}{\partial x_j} = -\rho g u_3 + \frac{\partial u_i \sigma_{ij}}{\partial x_j} - \frac{\partial q_j}{\partial x_j},\tag{3}$$

$$p = \rho RT,\tag{4}$$

where ρ is density, ρu_i is momentum per unit volume, $\rho E = \rho(c_v T + u_k u_k/2)$ is total energy per unit volume, p is pressure, T is temperature, R is gas constant for dry atmosphere, $\sigma_{ij} = \mu \left[(\partial u_i/\partial x_j + \partial u_j/\partial x_i) - \frac{2}{3}(\partial u_k/\partial x_k)\delta_{ij} \right]$, and $q_j = -\kappa \partial T/\partial x_j$. Here, c_v is specific heat for constant volume and δ_{ij} is the Kronecker delta. μ and κ are the

KOHMA ET AL. 3 of 22

21698996, 2024, 3, Downloaded from https://agupubs.onlinelibrary.wiley.com/doi/10.1029/2023JD039425, Wiley Online Library on [02/12/2024]. See the Terms and Cor

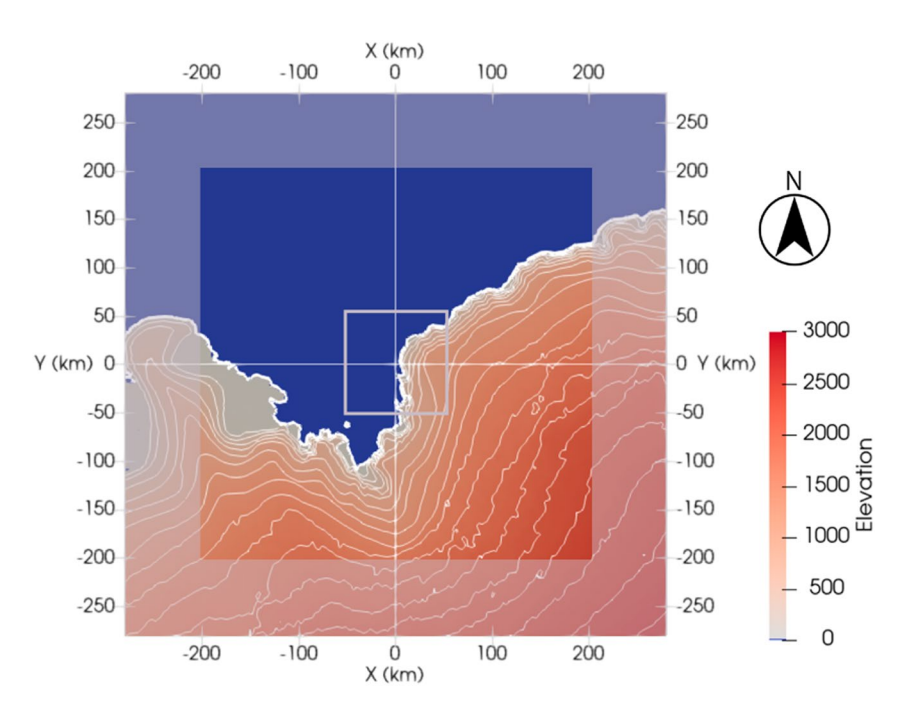


Figure 1. Terrain heights around Syowa Station in the Complex Geometry Compressible Atmospheric Model domain. Syowa Station is located on a small island at the center of the model domain. The contour interval is 150 m. The thick white contours indicate the coastline. A gray open rectangle indicates the central domain with a constant grid spacing of 250 m. The gray shaded area along the edge of the panel indicates the sponge layer.

dynamic viscosity and thermal conductivity, respectively. To include the influence of subgrid-scale turbulent processes, we employed the dynamic Smagorinsky subgrid-scale model (Germano et al., 1991; Moin et al., 1991). Thus both μ and κ consist of molecular and subgrid-scale components. The equations for the eddy viscosity, eddy conductivity, and turbulent kinetic energy coefficients are averaged over the horizontal planes, which is a standard treatment to obtain well-conditioned equations (Lund et al., 2020).

The computational horizontal domain is a square with a width of 560 km centered on Syowa Station (Figure 1). The horizontal grid spacing is 250 m within a central square with a width of 100 km (a gray rectangle in Figure 1) while outside of the central region, it increases gradually up to \sim 4.8 km at the horizontal boundary. The vertical domain extends from the ground to 96 km. The vertical grid spacing is 60 m below 48 km and is stretched up to about 500 m at the model top. The total computational mesh is $696 \times 696 \times 960$ in the zonal, meridional, vertical directions, respectively. Although the model domain includes the mesosphere as well as troposphere and stratosphere, this paper focuses on MWs and their responses observed below 30 km, and the GW responses at higher altitudes will be explored in another paper.

Another numerical simulation with a horizontal grid spacing of 125 m in the central region was also performed. The difference of the GW structure between 250 m-resolution and 125 m-resolution results is so small that the 250 m grid spacing is likely sufficient to capture the GW dynamics in the present case.

The model uses the low-storage, third-order Runge-Kutta time integration, and Δt is set to 0.2 s in the present experiment. The total integration time is 12 hr. Although the integration time is shorter than the spin-up time used in previous studies (e.g., Plougonven et al., 2013), the numerical simulation confirms that the primary wave patterns below an altitude of 10 km become approximately steady after 10 hr, while small-scale turbulent motion retains its transient nature.

3.2. Terrain

For the terrain around Syowa Station, we used the Radarsat Antarctic Mapping project v2 (RAMPv2) data set with a horizontal resolution of 200 m (Liu et al., 2015). The terrain is shown in Figure 1. Note that in the model domain, +x and +y directions are approximately eastward and northward, respectively. There is a steep terrain

KOHMA ET AL. 4 of 22

21698996, 2024, 3, Downloaded from https://agupubs.onlinelibrary.wiley.com/doi/10.1029/2023JD039425, Wiley Online Library on [02/12/2024]. See the Terms

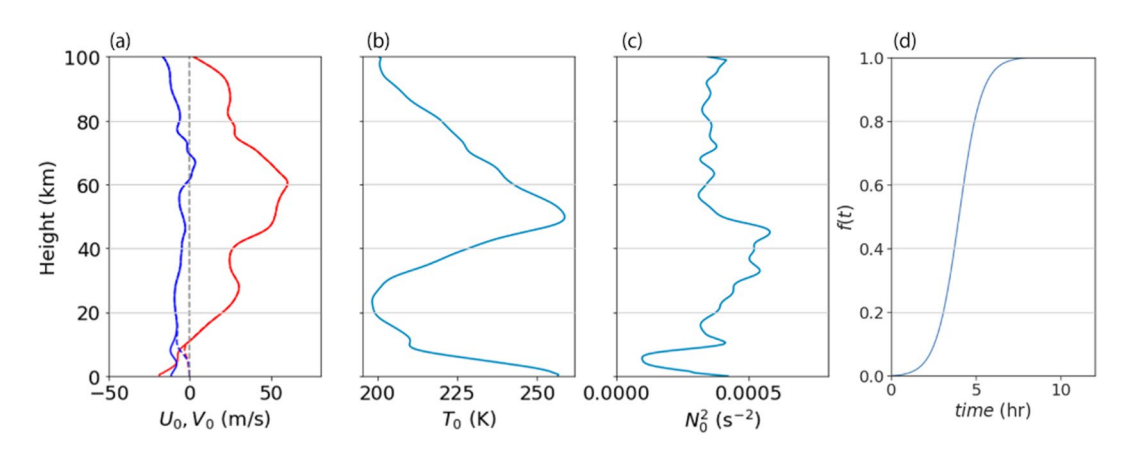


Figure 2. (a) Vertical profiles of U_0 (red) and V_0 (blue) over Syowa Station up to an altitude of 100 km. The broken curves indicate initial vertical profiles of U_0 and V_0 . Panels (b, c) same as panel (a) but for (b) T_0 and (c) N_0^2 . (d) The prescribed time variation of ramping f(t) for low-level U_0 and V_0 .

about 5 km east of Syowa Station, which is approximately aligned to the N-S direction. While Syowa Station is \sim 30 m above sea level, the terrain elevation is higher than 900 m at 50 km east of Syowa Station. The vertical mesh is distorted in the lower portion of the model domain to match the terrain. The distortion decreases gradually with height, and above 15 km, the distortion disappears completely.

3.3. Initial Conditions and Forcing

The background condition for the numerical experiment was given by a single vertical profile composed of two kinds of reanalysis data: the Modern-Era Retrospective Analysis for Research and Applications, version 2 (MERRA-2, Gelaro et al., 2017) and Japanese Atmospheric GCM for Upper Atmosphere Research-Data Assimilation System (JAGUAR-DAS; Koshin et al., 2020, 2022) data sets. Note that the top of MERRA-2 data set (0.1 hPa) is lower than the model top of the present numerical experiment, whereas the JAGUAR-DAS is not capable of realistically reproducing phenomena smaller than the synoptic scale ones in the troposphere due to its low horizontal resolution (T42). Vertical profiles from MERRA-2 and JAGUAR-DAS were smoothly connected around an altitude of 45 km; for example, the background zonal wind U_0 is given by

$$U_0(z) = W(z)U_{\text{MERRA2}}(z) + [1 - W(z)]U_{\text{J-DAS}}(z),$$
(5)

where $U_{\rm MERRA2}$ and $U_{\rm J-DAS}$ are zonal wind vertical profiles at the grid point nearest to Syowa Station averaged over 18 May 2021 from the MERRA-2 and JAGUAR-DAS, respectively. Here, $W(z)=(1+\tan h[(z-45\,{\rm km})/4\,{\rm km}])/2$. Background meridional wind $V_0(z)$ and temperature $T_0(z)$ were calculated similarly. Background vertical profiles are shown in Figure 2a–2c. The surface wind is from the ENE direction and its magnitude is 20.2 m s⁻¹. The background zonal wind is westward below 10 km while strong westerly jet is observed above $z=20\,{\rm km}$. The meridional wind is southward from the ground to 65 km altitude. The tropopause height is approximately 9 km, where the buoyancy frequency squared, $N_0^2=g/\theta_0\partial\theta_0/\partial z$, has a local maximum (\sim 0.47 × 10⁻⁴ s⁻²). Note also that N_0^2 has another local maximum (\sim 4 × 10⁻⁴ s⁻²) at the ground. There is no altitude range where the Richardson number $(N_0^2/[(dU_0/dz)^2+(dV_0/dz)^2])$ is less than unity (not shown), indicating that local instability from the background fields is unlikely to occur.

Following Lund et al. (2020), non-physical starting transients are minimized by initially damping the mean background horizontal winds toward zero in the lower portion of the model domain. The background winds U(z, t) and V(z, t) near the surface are then increased gradually in time according to:

$$U(z,t) = U_0(z)\{d(z) + [1 - d(z)]f(t)\},\tag{6}$$

where

$$d(z) = \frac{1}{2} \left[1 + \tanh\left(\frac{z - z_c}{z_w}\right) \right],\tag{7}$$

KOHMA ET AL. 5 of 22

21698996, 2024, 3, Downloaded from https://agupubs.onlinelibrary.wiley.com/doi/10.1029/2023JD039425, Wiley Online Library on [02/12/2024]. See the Terms and Condition

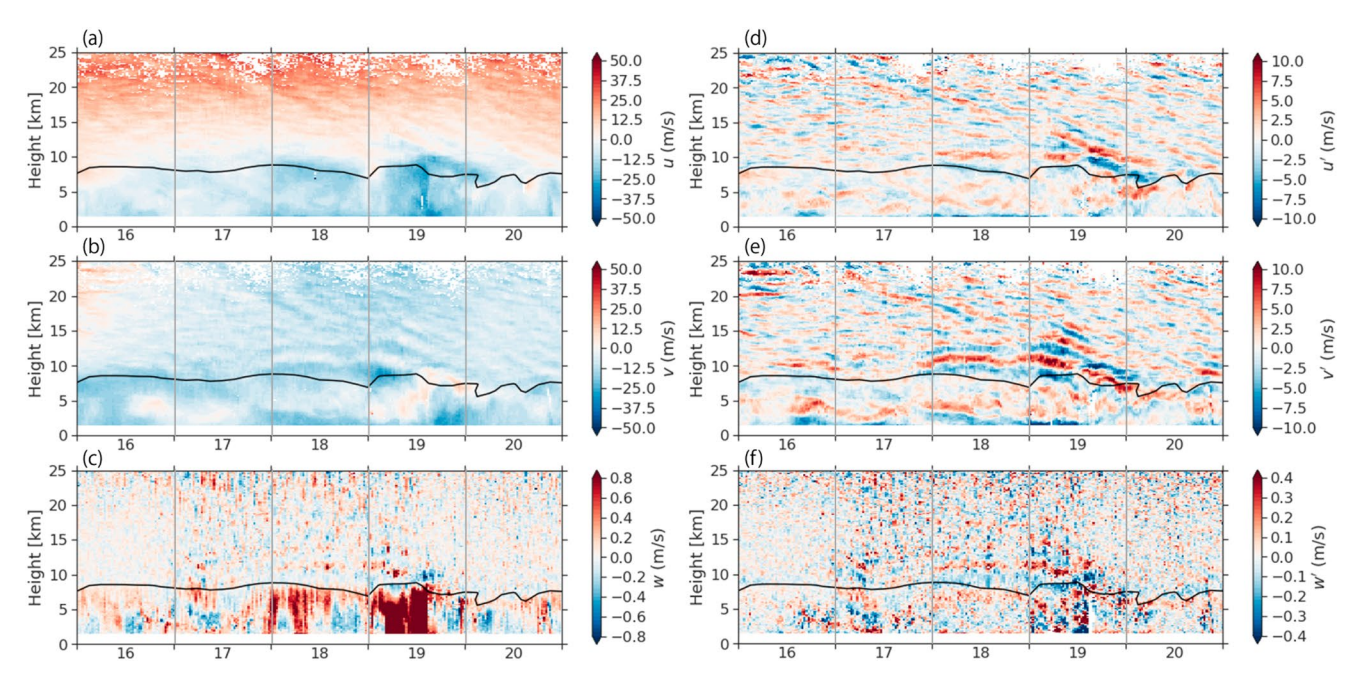


Figure 3. (a–c) Time-height sections of (a) u, (b) v, and (c) w on 16–20 May 2021. Black curves indicate isolines of potential vorticity of -2×10^{-6} K m² kg⁻¹ s⁻¹ from ERA5, which indicate the dynamical tropopause height. Panels (d–f) same as panels (a–c) but for wind fluctuations (d) u', (e) v', and (f) w'.

$$f(t) = \min\left\{\frac{1}{2}\left[1 + \tanh\left(\frac{t - t_m}{t_m/3}\right) / \tanh(3)\right], 1\right\},\tag{8}$$

and where $t_m = 4$ hr, $z_c = 8$ km, and $z_w = 4$ km. The background meridional wind V(z, t) is given similarly. The vertical profiles of the background winds at the initial time step are shown by the broken curves in Figure 2a. The ramp function f(t) gradually increases to unity by t = 8 hr (Figure 2d), and $[U(z,t),V(z,t)] = [U_0(z),V_0(z)]$ after t = 8 hr.

3.4. Boundary Conditions

A characteristic boundary condition with numerical sponge layers was used at the upper and horizontal boundaries to prevent reflection of GWs and acoustic waves at the boundaries. The implementation of the sponge layer is described in Lund et al. (2020). The sponge layer has the hyperbolic-tangent shape with a width of 80 km (4 km) at the lateral (upper) boundaries. The time constants for damping are 128 and 4 s for the lateral and upper boundaries, respectively. At the lower boundary, free-slip and adiabatic boundary conditions were employed. This neglects the strong radiative cooling over the surface of the Antarctic continent, which is known to the main driver of katabatic winds observed along the coast of Antarctica (e.g., Parish & Bromwich, 1987).

4. Observations From the PANSY Radar

4.1. Winds and Momentum Fluxes

Figures 3a–3c show time-height sections of zonal, meridional, and vertical winds (u, v, w) from the PANSY radar on 16–20 May 2021. Southward winds dominate from the lowest level up to 25 km altitude, while the zonal winds are predominantly westward at 1.5–10 km altitudes, and eastward above 12 km. Strong vertical wind disturbances with amplitudes greater than 0.8 m/s were observed below 8 km altitudes on 18–19 May. The upper limit of the disturbances corresponds largely to the tropopause height (black curves). The time evolution of wind fluctuations $v' \equiv (u', v', w')$ is shown in Figure 3d–3f. Here, the background wind is defined as the wind components with a vertical wavelength longer than 6 km. On 18 May, a wave-like pattern was observed for u', v', and w' at z = 10–15 km, and the phase of the wave was steady for about a day. The amplitude of v' is 5–6 m s⁻¹ at z = 11–14 km, which is larger than that of u' (<1.5 m s⁻¹). The negative maximum of v' are observed at altitudes of 10 and 13 km, which suggests the vertical wavelength is approximately 3 km. The steadiness of the wave phase indicates that the wave pattern is attributable to orographic GW. Hodograph analysis (e.g., Minamihara

KOHMA ET AL. 6 of 22

21698996, 2024, 3, Downloaded from https://agupubs.onlinelibrary.wiley.com/doi/10.1029/2023JD039425, Wiley Online Library on [02/12/2024]. See the Terms and Condition

of use; OA articles are governed by the applicable Creative Commons License

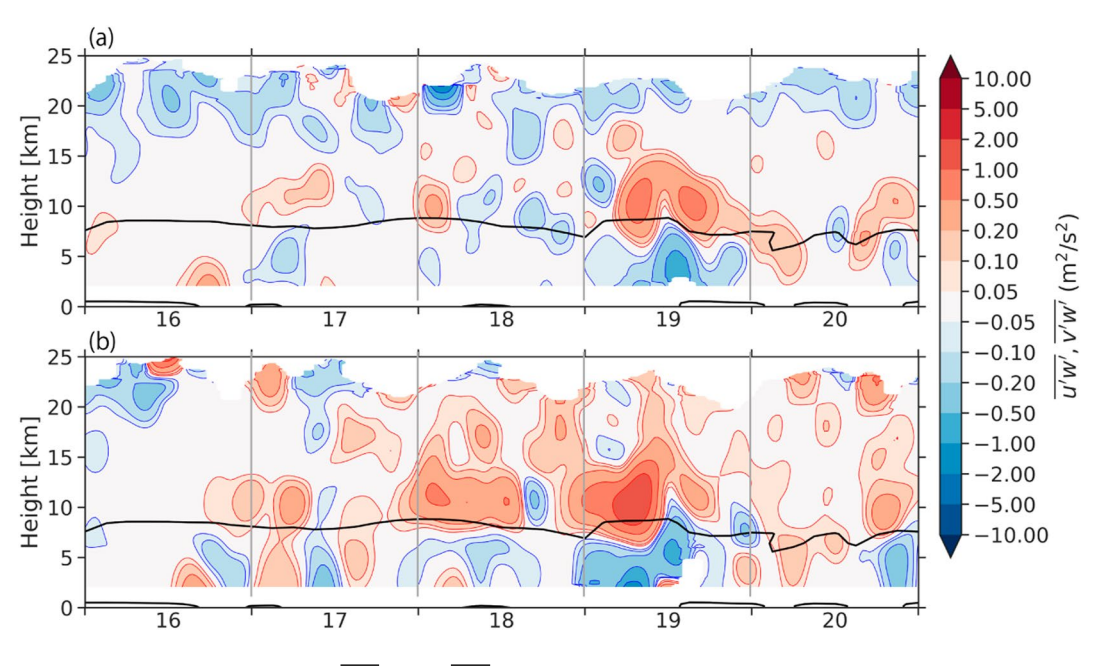


Figure 4. Time-height sections of (a) $\overline{u'w'}$ and (b) $\overline{v'w'}$ on 16–20 May 2021. Black curves indicate isolines of potential vorticity of 2×10^{-6} K m² kg⁻¹ s⁻¹ from ERA5. Colors are almost logarithmic scale.

et al., 2018; Yoshiki & Sato, 2000) in the height range of 10–15 km shows (a) that the hodograph depicts counterclockwise rotation with height, indicative of upward group velocity, (b) that the horizontal wavenumber vector is oriented in the N-S direction, and (c) that the vertical wavelength of the wind pattern is approximately 2–3 km (not shown).

In the troposphere, the wave pattern is not clear on 18 May. This is likely due to longer vertical wavelength in the troposphere that the GW has owing to smaller background N^2 compared to the stratosphere. According to the linear wave theory, when the background field is both steady and horizontally uniform, ground-based frequency, ω , and horizontal wavenumber, k, remain constant along the ray, namely path of wave packet propagation (e.g., Andrews et al., 1987). For internal hydrostatic GWs, the (local) dispersion relation is given by $(\omega - Uk)^2 = (k/mN)^2$, where U = U(z) is the background horizontal wind oriented to the horizontal wavenumber vector (N-S direction). The buoyancy frequency N are 1.0×10^{-2} s⁻¹ and 2.1×10^{-2} s⁻¹ at altitudes of 4 and 11 km, respectively, while the background meridional winds do not exhibit significant variation across the tropopause height (Figure 2). For upward propagating wave packets to maintain constant ω and k, the vertical wavelength in the lower stratosphere should be approximately a half of that in the troposphere. There are local minima for the unfiltered meridional winds (v) at 2 and 8.5 km on 18 May (Figure 3b), suggesting that the GW wavelength in the troposphere is about 6.5 km. Since the background winds can also vary with a similar vertical scale, it is difficult to distinguish long-period waves with such a large vertical wavelength from the background using radar observations at a single location. Note that another wave pattern was observed in the lower stratosphere on 19 May. The wave pattern is presumably linked to strong upward motion below an altitude of 8 km and the associated vertical displacement of the tropopause. Since the phase of the wave pattern descends with time, further examination may be necessary in order to determine the wave source.

Figure 4 shows time-height sections of zonal and meridional momentum fluxes. The estimation method proposed by Vincent and Reid (1983) has been used, and smoothing with a width of 6 hr and 6 km was applied for clear visualization. On 18 May, strong positive $\overline{v'w'}$ with a maximum of 1.0 m² s⁻² is observed at altitudes of 8–15 km, while $\overline{u'w'}$ is wake and does not show a systematic pattern in the lower stratosphere. Since the background meridional wind is southward, the sign of $\overline{v'w'}$ is consistent with the linear theory of the orographic GW.

4.2. Turbulent Energy Dissipation Rates

Figure 5 shows a vertical profile of the daily-averaged ε on 18 May 2021. Below z=3 km, a strong turbulent layer of ε larger than 10^{-3} m² s⁻³ was observed, which is an order of magnitude larger than the annual mean (Kohma et al., 2019). While ε is small in an altitude range of 5–8 km compared to that in the low-level turbulent layer,

KOHMA ET AL. 7 of 22

.com/doi/10.1029/2023JD039425, Wiley Online Library on [02/12/2024]. See the Terms

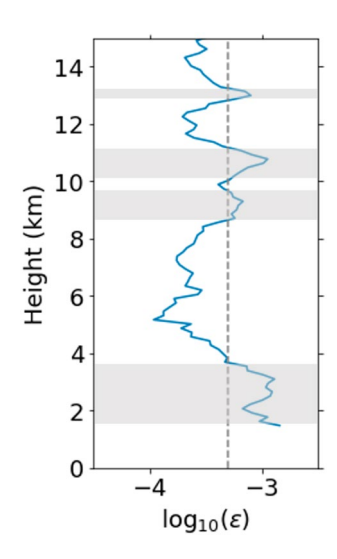


Figure 5. A vertical profile of $\log_{10}(\varepsilon)$ averaged over 18 May 2021. A vertical broken line indicates $5 \times 10^{-4} \text{ m}^2/\text{s}^{-3}$.

several peaks of ε are observed in the lower stratosphere, namely at 9.2, 10.8, and 13 km, indicating a multi-layer structure of strong turbulence.

5. Numerical Simulations

Figures 6a and 6b shows horizontal maps of w at an altitude of 7.5 km at t = 9 and 12 hr. Movies of the time evolution of w in the horizontal plane are included for reference in the accompanying Supporting Information S1. On the continental coast northeast of Syowa Station, ship wave patterns with an amplitude of ~ 0.5 m s⁻¹ are present at 9 and 12 hr. The phase and amplitude of the wave pattern for both plots are quite similar. The results suggest generation of MW from small-scale uneven terrain along the coast of the continent under the background surface winds from the ENE. To the south of Syowa Station, there are vertical wind disturbances with an amplitude greater than 1 m s⁻¹. The wave phase lines are approximately aligned with the coast of steep terrain. Furthermore, small-scale turbulent disturbances are prominent in the region southeast to the west of Syowa Station, particularly at t = 12 hr. Note that the magnitude of the vertical wind over Syowa Station is approximately 2 m s⁻¹, which is slightly larger than or comparable to observation from the radar on 18 May (Figure 3c).

Horizontal maps of w at z = 15 km are shown in Figures 6c and 6d. Although wave patterns are observed northeast of Syowa Station at an altitude of 15 km,

they are significantly different from those at 7.5 km. For example, wave structures with wavenumber vectors pointing to the E-W direction are not evident at 15 km. It is interesting to note that, while the large-amplitude disturbances with horizontal wavelengths shorter than \sim 15 km are observed southwest of Syowa Station at 9 hr, wave patterns with a horizontal wavelength of \sim 30 km and a wavenumber vector directed to the N-S direction are evident in the regions west of Syowa Station at 12 hr.

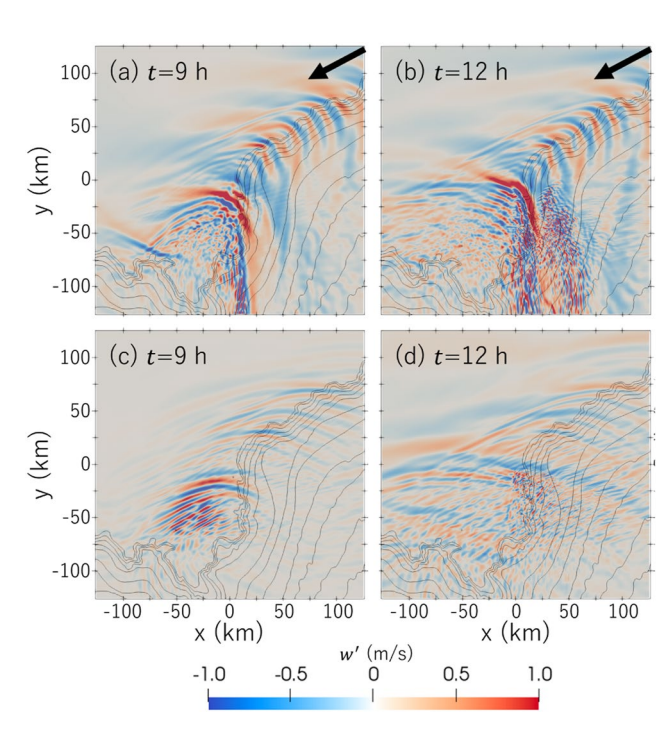


Figure 6. (a, b) Horizontal maps of w at an altitude of 7.5 km at (a) t = 9 hr and (b) 12 hr. A black arrow at the upper-right corner of each panel indicates the direction of surface wind. Gray contour indicates the terrain height with an interval of 150 m. Panels (c, d) same as panels (a, b) but for w at an altitude of 15 km.

To examine the temporal change in horizontal structure of the MW with altitude, horizontal maps of w at 5, 8, 12, 16, 20, and 24 km at 12 hr are shown in the left column of Figure 7. The right column of Figure 7 shows two-dimensional horizontal power spectra $P_w(k, l)$ calculated from w in the $100 \text{ km} \times 100 \text{ km}$ horizontal domain at 12 hr, where k and l are zonal and meridional wavenumbers, respectively. The power spectra are calculated from w fields vertically interpolated with an interval of 60 m, and then averaged over a vertical width of about 4 km. Below 10 km, waves with horizontal wavelengths longer than 5 km are dominant, and the orientation of horizontal wavenumber vector $\mathbf{k}_{h} = (k, l)$ with the N-S, NNE-SSW, NE-SW, ENE-WSW, and E-W directions are observed. It is interesting to note that reduction of P_{w} for k_{b} oriented to the E-W and ENE-WSW directions is observed in the altitude range of 10-14 km. Furthermore, above 14 km, amplitudes of waves with $k_{\rm h}$ oriented to the NE-SW direction are small compared to those below 14 km. In other words, prevailing waves have NNW-SSE oriented k_h above 14 km, despite P_{w} for k_{h} oriented to NNW-SSE being smaller in the altitude range of 3-7 km than those with other directions.

According to linear GW theory, the propagation characteristics of MWs are dictated by the vertical wavenumber $m \equiv 2\pi/\lambda_z$, where m^2 is given by the dispersion relation as

$$m^2 = \frac{N^2}{U_h^2} - \frac{U_{hzz}}{U_h} + \frac{U_{hz}}{U_h H} - k_h^2 - \frac{1}{4H^2},$$
 (9)

where U_h is the component of background horizontal winds in the direction of k_h , k_h is horizontal wavenumber, and H is density scale height (e.g., Lund et al., 2020). Linear theory indicates that large m^2 leads to small upward group velocity and that m^2 becomes infinite at the critical level. Figure 8a

KOHMA ET AL. 8 of 22

21698996, 2024. 3, Downloaded from https://agupubs.onlinelibrary.wiley.com/doi/10.1029/2023/D039425, Wiley Online Library on [02/12/2024]. See the Terms and Conditions (https://onlinelibrary.wiley.com/derms-and-conditions) on Wiley Online Library for rules of use; OA articles are governed by the applicable Creative Commons License

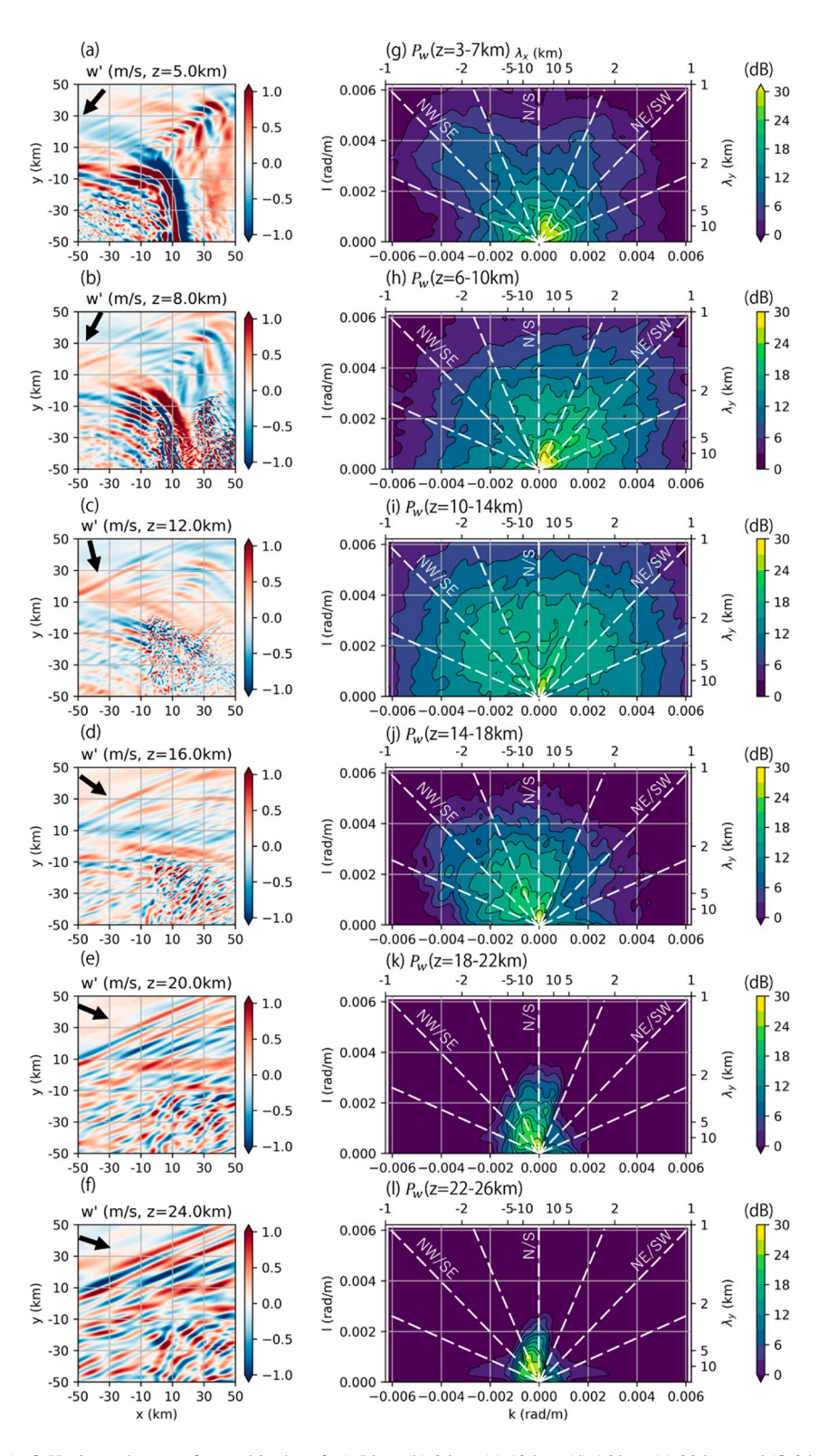


Figure 7. (a–f) Horizontal maps of w at altitudes of (a) 5 km, (b) 8 km, (c) 12 km, (d) 16 km, (e) 20 km, and (f) 24 km at t = 12 hr. Arrows at the upper-left corner indicate the directions of background wind at each height. (g–l) Horizontal power spectrum of w at altitude ranges of (g) 3–7 km, (h) 6–10 km, (i) 10–14 km, (j) 14–18 km, (k) 18–22 km, and (l) 22–26 km. The white broken lines serve as reference lines indicating the orientations of ENE-WSW, NE-SW, NNE-SSW N-S, SSE-NNW, SE-NW, and ESE-WNW.

KOHMA ET AL. 9 of 22

21698996, 2024, 3, Downloaded from https://agupubs.onlinelibrary.wiley.com/doi/10.1029/2023JD039425, Wiley Online Library on [02/12/2024]. See the Terms and Cor

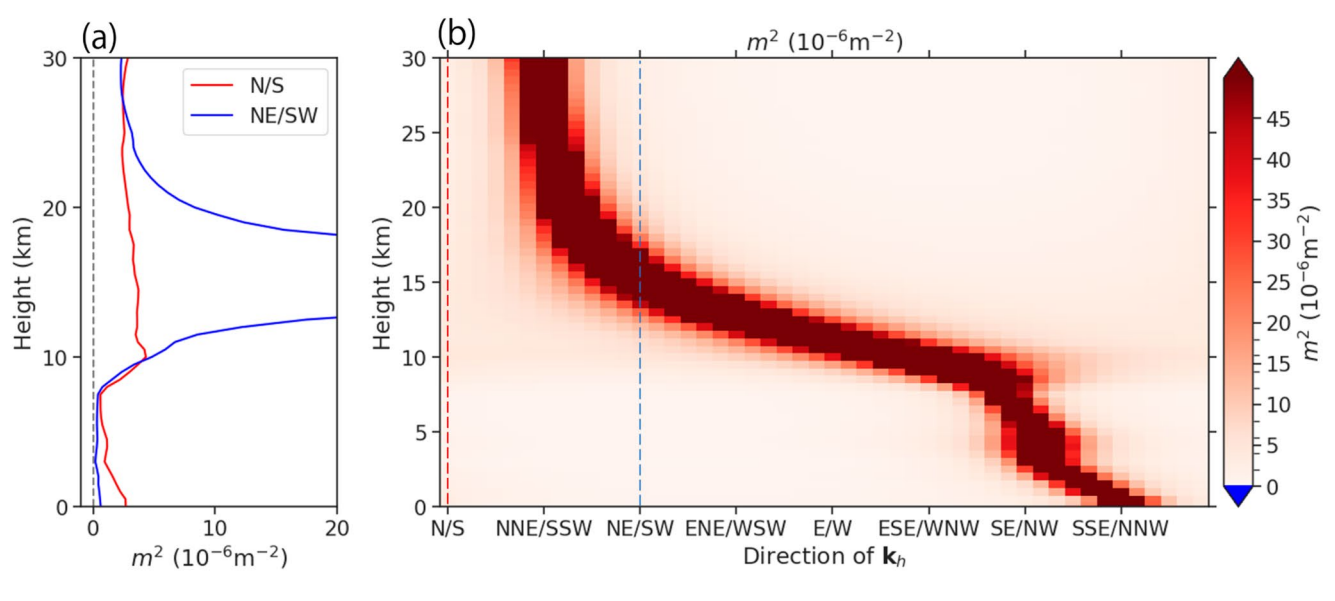


Figure 8. (a) Vertical profiles of m^2 for horizontal wavelength of 30 km for k_h oriented to N-S (red) and NE-SW (blue). (b) The values of m^2 for horizontal wavelength of 30 km for different directions of k_h as a function of height. The calculation of m^2 is performed every $\pi/48$ rad. A red and blue vertical broken lines indicate the N-S and NE-SW orientations, respectively.

shows the vertical profiles of m^2 calculated from the background wind profile (Figure 2) with $k_{\rm h}=30$ km for $k_{\rm h}$ oriented to N-Sand NE-SW. While there is a critical level for MW with $k_{\rm h}$ oriented to the NE-SW direction in the altitude range of 15–18 km, for waves directed to N-S, m^2 have finite positive values in the altitude range of 1–30 km. Figure 8b shows the m^2 values calculated every $\pi/48$ rad. It is found that there is no critical level for waves directed to NS and SSENNW up to an altitude of 30 km. Thus, the altitudinal variation of P_w , namely predominant horizontal structure of GW, is likely attributable to the critical-level filtering effect in the directional shear.

Figure 9a-9c shows y-z sections of w along x = 0 km at 8, 9, and 12 hr. Above Syowa Station (black vertical lines), at t = 12 hr, positive values of w are observed at altitudes of 2.0, 8.5, 11.5, and 14.5 km. This suggests that a wave pattern with a vertical wavelength of ~3 km is observed at altitudes higher than 9 km whereas the vertical wavelength is longer than 6 km in the troposphere. The wave pattern of w in the lower stratosphere looks like those observed on 18 May 2021 from the radar observations (Figure 3). For y < 0 km, strong vertical wind disturbances are observed in the troposphere all the time. Interestingly, above an altitude of 10 km, the small-scale disturbances of w appear in y < 0 km at t = 12 hr. To examine the turbulence generation at these altitudes, the same sections but for the vorticity magnitude $|\xi|$ are shown in Figures 9d–9f. Movies of the time evolution of $|\xi|$ in the same section are included for reference in the accompanying Supporting Information S1. A strong turbulent layer is observed near the surface south of Syowa Station (i.e., y < 0 km), which has been continuously observed after 7 hr. The depth of surface turbulent layer is about 1.5 km. Above Syowa Station, there are layers of large of 11–12 km and around 13 km, indicative of MW breaking. It should be noted that the multi-layer structure of strong ε in the lower stratosphere is also seen in the radar observations (Figure 5) although the heights of the turbulent layers are not exactly the same as those seen in the numerical simulation. For y < -20 km, z = 8-11 km, patches of large ξ are observed. Figures 9g-9i shows $|\xi|$ along x = +50 km, which is upwind of x = 0 km for the lower stratosphere. At t = 9 hr, the turbulent billows tend to develop along the high-shear region associated with the GW phase in the altitude range of 9-11 km. The turbulent billows are advected westward and result in patches of large $|\zeta|$ in the section along x = 0 km (Figures 9b) and 9c). It is worth noting that the altitude range of 9–13 km includes the critical levels for stationary GWs like MWs with k_h oriented to the E-W, ENE-WSW, and NE-SW directions (Figure 8), which should lead to GW breaking for these modes.

The three-dimensional structure of $|\xi|$ above Syowa Station at 9–12 km altitudes is shown as isovalue surface where $|\xi|$ is 10^{-4} s⁻¹ in Figure 10. Note that the background wind in this altitude range is largely from the +y direction. There are many horseshoe-shaped or hairpin-shaped vorticity tubes for y < 0 km, indicating streamwise-aligned counter-rotating rolls. The horseshoe-shaped vorticity tubes are known to be a typical characteristic of the early stage of GW instabilities (e.g., Andreassen et al., 1998; Fritts et al., 1998, 2009).

KOHMA ET AL. 10 of 22

21698996, 2024, 3, Downloaded from https://agupubs.onlinelibrary.wiley.com/doi/10.1029/2023JD039425, Wiley Online Library on [02/12/2024]. See the Terms and Conditions (https://onlinelibrary.wiley.com/terms-and-conditions) on Wiley Online Library for rules of use; OA articles are governed by the applicable Creative Commons Licensia

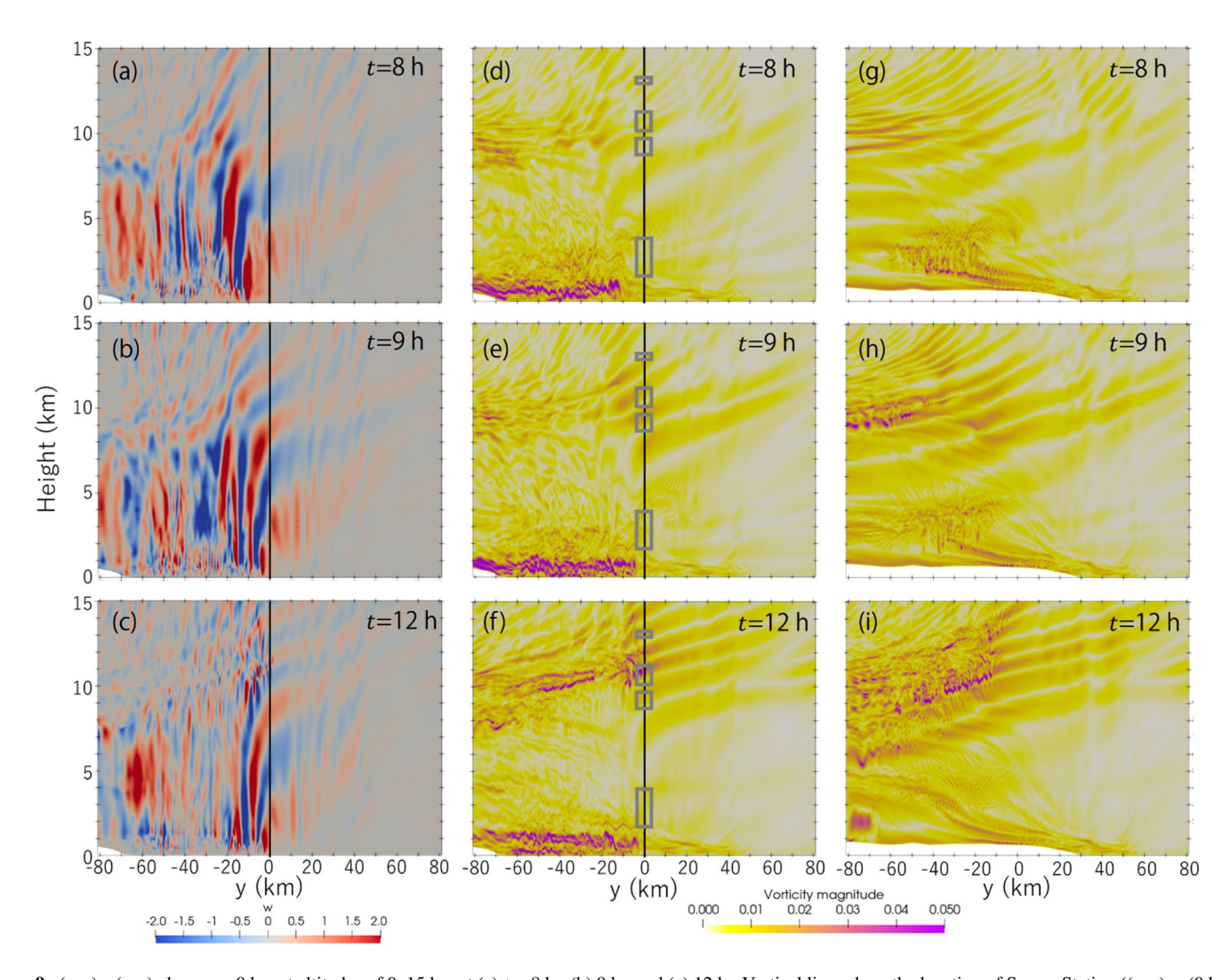


Figure 9. (a–c) w(y, z) along x = 0 km at altitudes of 0–15 km at (a) t = 8 hr, (b) 9 hr, and (c) 12 hr. Vertical lines show the location of Syowa Station ((x, y) = (0 km, 0 km)). Panels (d–f) same as panels (a–c) but for $|\zeta|(y, z)$ along x = 0 km. Gray rectangles indicate the height ranges of ε estimated from the radar greater than 5×10^{-4} m² s⁻³, which is highlighted in Figure 5. Panels (g–i) same as panels (d–f) but for $|\zeta|(y, z)$ along x = +50 km.

Figures 11b–11g shows isentropic (potential temperature) surfaces for 260 and 300 K at t = 8, 10, and 12 hr. Movies depicting the evolutions of the isentropic surfaces are included for reference in the accompanying Supporting Information S1. At 300 K, turbulent disturbances on a small scale are observed along the phase line extending southward, indicating GW breaking around the critical level (Figure 9). GWs with N-S phase lines can be attributed

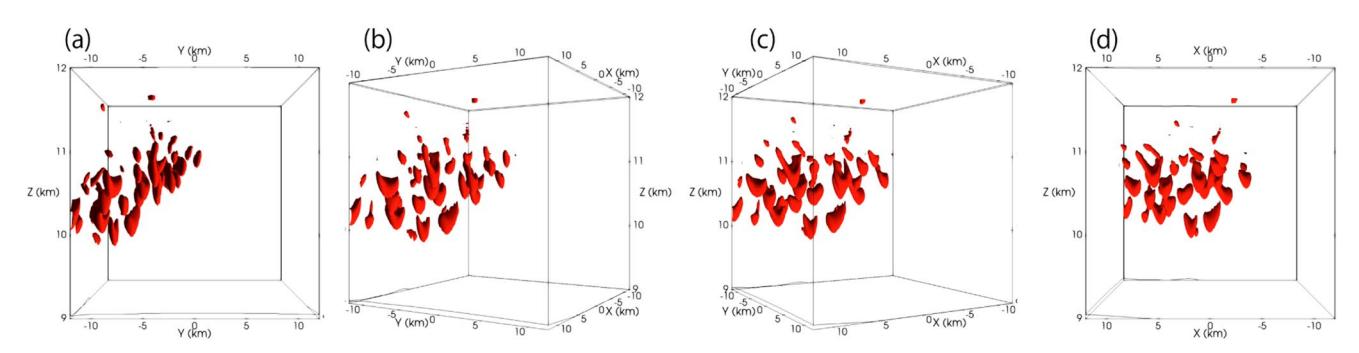


Figure 10. (a) Isovalue surfaces where $|\xi|$ is 10^{-4} s⁻¹ at t = 12 hr at altitudes of 9–12 km for the central domain with a width of 20 km shown from +x direction. Panels (b–d) same as panel (a) but for surface rotated clockwise around the z-axis by 30° each.

KOHMA ET AL. 11 of 22

21698996, 2024, 3, Downloaded from https://agupubs.onlinelibrary.wiley.com/doi/10.1029/2023JD039425, Wiley Online Library on [02/12/2024]. See the Terms and Condition to downslope winds from the ENE along the coastal terrain that extends in the N-S direction (Figure 11a). After t = 8 hr, a drastic rise in the isentropic surface of 260 K near the coast by 0.5–0.8 km suggests the presence of a hydraulic jump downwind of the steep slope. Figure 12 shows x-z sections of θ and u along y = -20 km. A sharp rise in the isentropic surfaces is observed on the downslope of the continent after t = 8 hr. East of the jump, strong downslope winds are observed, whereas west of the jump, the magnitude of u near the ground is quite small. These features are typical characteristics of a hydraulic jump (e.g., Durran, 1986, 1990). Additionally, at t = 8 hr, a low-level turbulent wake is observed, spreading downwind of the hydraulic jump (Figure 11b). At later times the turbulent wake front progress in the +y direction (northward), resembling a bore (e.g., Rottman & Simpson, 1989). At t = 12 hr, the front appears steady, and the resultant phase lines are largely straight and extends in the E-W direction. Interestingly, the E-W extending turbulent wake front produces a structure similar to that of the 300-K isentropic surface with a horizontal wavelength of ~30 km to the west of Syowa Station.

To investigate the relation between the low-level turbulent wake and upper-level wave structure, vertical sections of potential temperature θ and meridional wind disturbances v' along x = -50 km are presented in Figure 13. Here, v' is defined as a departure from the large-scale fields with a meridional wavelength longer than 60 km. Near the surface, the northward progression of the isentropic surface hump is observed at t = 7-10 hr. The vertical gradient of θ is small below the elevated isentropic surfaces, indicating strong vertical mixing within the bottom layer. Since sharp changes in θ across the front are evident near the surface, the propagation of the front of the turbulent wake is considered to be associated with a gravity current (or density current). Above the turbulent wake front, a wave structure for v' is observed, with vertical wavelength of ~ 8 km in the troposphere but reducing to ~3 km in the lower stratosphere. It should be noted that another wave pattern is observed on the windward side of the hump, which is associated with GWs generated along the Antarctic coast northeast of Syowa Station and advected by the background winds (Figure 11).

Figure 14 shows the same vertical sections but for meridional momentum fluxes v'w'. Positive v'w' are also prominent above the turbulent wake front. Notably, the lower ends of the v' wave structure of and positive v'w'move following northward progression of the turbulent wake front. Since the background wind is from ENE, it stands to reason that the adiabatic lift of an airmass along the isentropic surface hump results in GW generation.

Figure 15 displays zonal and meridional momentum fluxes associated with GWs. Here, GW components are defined as departures from large-scale fields with zonal and meridional wavelengths longer than 60 km. Spatial averaging is applied to the momentum fluxes in the zonal and meridional directions using a low-pass filter with a cutoff length of 60 km. While $\overline{u'w'}$ shows positive values of \sim 0.2 m² s⁻² at 12 km and small negative values at 18 km over Syowa Station, $\overline{v'w'}$ exhibits large positive values at both altitudes. The height variation of the sign of $\overline{u'w'}$ is consistent to power spectra of w and the wave filtering effect of background winds (Figures 7 and 8). At 12 km, the magnitude of positive $\overline{v'w'}$ is up to 1.0 m² s⁻², which is as large as that observed by the radar (Figure 4b). The positive v'w' extends to the west of Syowa Station, which is roughly aligned to the front of the isentropic surface hump near the ground (Figure 11d). These results indicate that the significant northward momentum fluxes observed over Syowa Station are likely due to GW generated from the gravity current front.

6. Discussion

In the present simulation, GWs with a horizontal wavelength of ~30 km are seen west of Syowa Station in the lower stratosphere, which explains the positive meridional momentum fluxes observed over Syowa Station. The meridional wavelength λ_{u} can be estimated from the radar observations. Using the continuity equation, λ_{u} is given by:

$$\lambda_y \approx \left| \frac{2\pi}{m} \right| \times \sqrt{\overline{v'^2}/\overline{w'^2}},$$
 (10)

conditions) on Wiley Online Library for rules of use; OA articles

where a term related to the density scale height is ignored, and the horizontal wavenumber vector is assumed to be oriented to the N-S direction. The radar observations showed wave structure in v' and w' with a vertical wavelength of 2–3 km and amplitudes of 5–6 m s⁻¹ and 0.2–0.3 m s⁻¹, respectively, at 11–14 km altitudes (Figures 3e and 3f). Thus, the meridional wavelength is estimated to be 38-69 km, which is slightly larger but comparable to the wavelength seen in the numerical simulation.

One of the interesting characteristics of the GWs radiated from the turbulent wake front is that the horizontal wavenumber vector is not aligned with the terrain slope east of Syowa Station, but aligned with the isentropic surface hump near the surface. Figure 16 shows a horizontal map of θ at an altitude of 0.5 km at t = 12 hr with

KOHMA ET AL. 12 of 22

21698996, 2024, 3, Downloaded from https://agupubts.onlinelibrary.wiley.com/doi/10.10292023JD039425, Wiley Online Library on [02/12/2024]. See the Terms and Conditions (https://onlinelibrary.wiley.com/doi/10.1029/2023JD039425, Wiley Online Library on [02/12/2024]. See the Terms and Conditions (https://onlinelibrary.wiley.com/doi/10.1029/2023JD039425, Wiley Online Library on [02/12/2024]. See the Terms and Conditions (https://onlinelibrary.wiley.com/doi/10.1029/2023JD039425, Wiley Online Library on [02/12/2024]. See the Terms and Conditions (https://onlinelibrary.wiley.com/doi/10.1029/2023JD039425, Wiley Online Library on [02/12/2024]. See the Terms and Conditions (https://onlinelibrary.wiley.com/doi/10.1029/2023JD039425, Wiley Online Library on [02/12/2024]. See the Terms and Conditions (https://onlinelibrary.wiley.com/doi/10.1029/2023JD039425, Wiley Online Library on [02/12/2024]. See the Terms and Conditions (https://onlinelibrary.wiley.com/doi/10.1029/2023JD039425, Wiley Online Library.wiley.com/doi/10.1029/2023JD039425, Wiley Online Library.wiley.com/doi/10

and-conditions) on Wiley Online Library for rules of use; OA articles are governed by the applicable Creative Commons Licenses

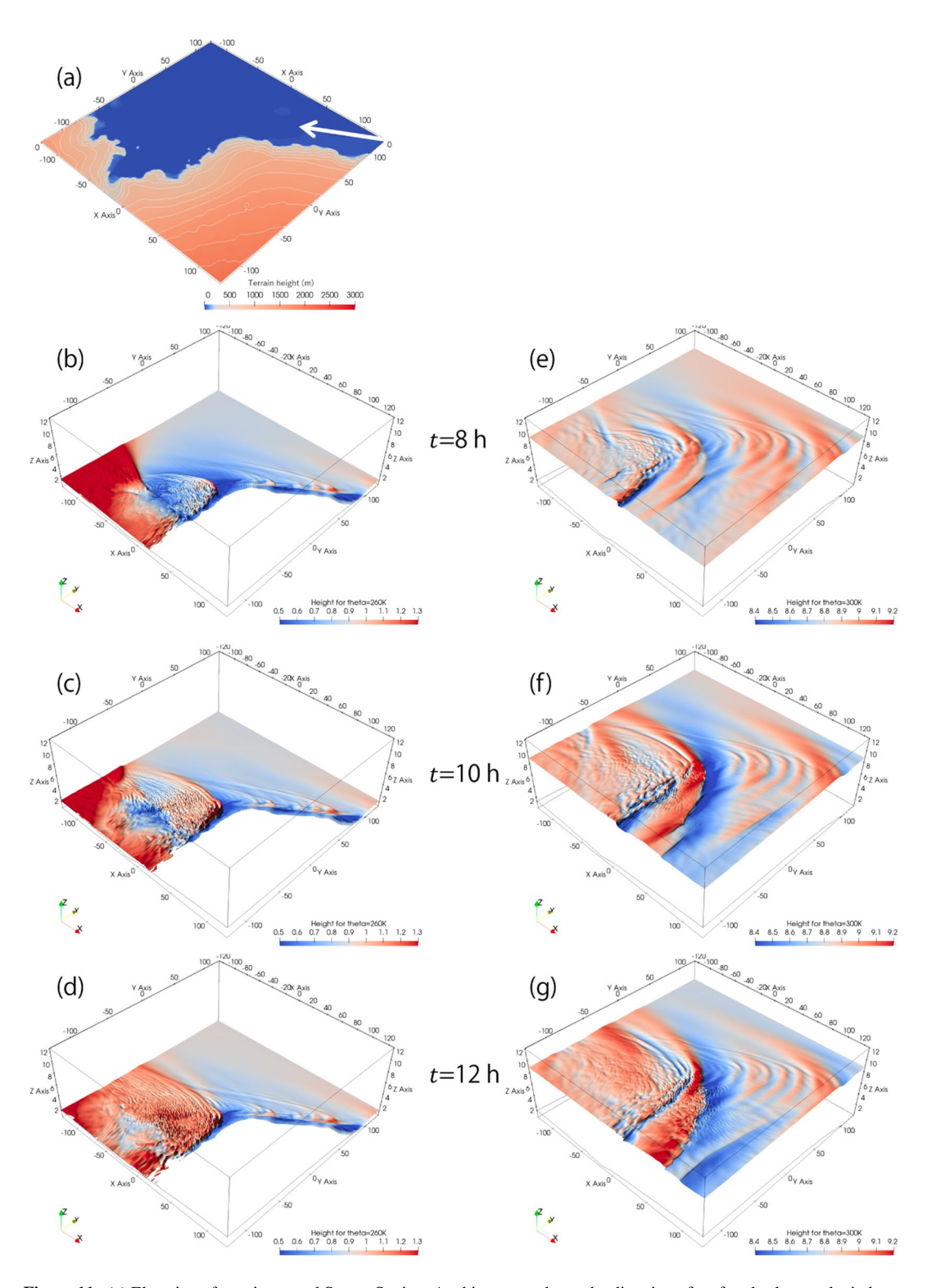


Figure 11. (a) Elevation of terrain around Syowa Station. A white arrow shows the direction of surface background wind $(U_0(0), V_0(0))$. (b–d) Isentropic surface for 260 K at (b) t = 8 hr (c) 10 hr, and (d) 12 hr. The color indicates the height of the isentropic surface. Panels (e–g) same as panels (b–d) but for isentropic surface for 300 K.

streamlines of surface horizontal winds. It is found that the isentropic surface front extends almost straight in E-W direction (indicated by a white broken line) and that the surface wind (a thick black arrow) crosses the front with a finite angle α (=41°-50° as shown in Figure 16), indicating adiabatic lift of an airmass across the front.

KOHMA ET AL. 13 of 22

21698996, 2024, 3, Downloaded from https://agupubs.onlinelibrary.wiley.com/doi/10.1029/2023JD039425, Wiley Online Library on [02/12/2024]. See the Terms

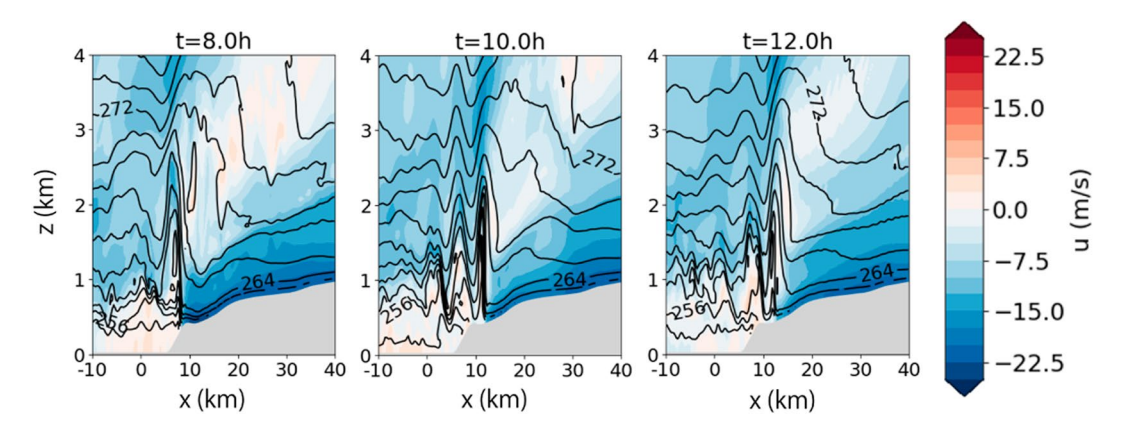


Figure 12. Vertical sections of θ (contour) and u (color) at altitudes of 0–5 km along y = -20 km at t = 8, 10, and 12 hr. The contour interval is 2 K. The gray region indicates terrain.

If the elevated isentropic surface, caused by the hydraulic jump occurring at the steep terrain, were advected passively, the front should be aligned to the surface wind vector (i.e., $\alpha = 0^{\circ}$). In that case, the uplift of airmass, and thus GW radiation, at the front would not occur. Therefore, it is interesting to consider the mechanism that determines α .

To continue the discussion, we assume that the propagation speed of the front relative to the background wind is determined by the propagation speed of the gravity current. Since the front does not move much after t = 10 hr (Figure 13), the ground-based speed of the front can be regarded as zero, and thus the steady state of the front is satisfied, while the turbulent wake downwind of the front shows a transient nature. From the analogy to shock waves, α can be regarded as a Mach angle, α_s , which is the half angle of the shock cone radiating from the edge of an object under the flow moving at a velocity V greater than the speed of sound c_s (e.g., Landau & Lifshitz, 1987). Since the Mach angle is given by $\alpha_s = \sin(c_s/V)$, α is estimated by the following equation:

$$\alpha = \operatorname{asin}(c_{\rm gc}/U_{\rm surf}),\tag{11}$$

where $c_{\rm gc}$ is the propagation speed of gravity current, and $U_{\rm surf}$ is the horizontal surface wind upwind of the front. Following the layer theories of downslope winds (R. B. Smith, 2019), $c_{\rm gc}$ is related to reduced gravity $g'=g\frac{(\theta_{\rm up}-\theta_{\rm down})}{\theta_{\rm cur}}$ (Benjamin, 1968), and thus,

$$c_{\rm gc} = \sqrt{2g'H_{\rm gc}},\tag{12}$$

where $\theta_{\rm up}$ ($\theta_{\rm down}$) denotes potential temperature upwind (downwind) of the front, and $H_{\rm gc}$ is the depth of the gravity current (see Figure 17a). Figure 17b shows vertical profiles of θ at t=12 hr at points A and B in Figure 16. Note that points A and B correspond to upwind and downwind of the front, respectively. It is found that the difference between $\theta_{\rm A}$ and $\theta_{\rm B}$ is larger than 1 K below an altitude of 1.0 km while the vertical profiles are almost coincident in the altitude range of 1.1–2.5 km. Here, $\theta_{\rm up}$ and $\theta_{\rm down}$ are calculated as follows:

$$\theta_{\rm up} = \frac{1}{H_{\rm gc}} \int_{0}^{H_{\rm gc}} \theta_{\rm A} dz, \theta_{\rm down} = \frac{1}{H_{\rm gc}} \int_{0}^{H_{\rm gc}} \theta_{\rm B} dz, \tag{13}$$

where $H_{\rm gc}$ is set to 1.0 km. From Equation 12, the propagation speed of the gravity current is given by 12 m s⁻¹. The speed of horizontal surface wind is 18 m s⁻¹ at point A, and thus, from Equation 11, $\alpha = 43^{\circ}$, which is consistent with the value observed in Figure 16 ($\alpha = 41^{\circ}-50^{\circ}$). We also found that the change in $H_{\rm gc}$ from 0.8 to 2.0 km leads to that of α with a range of 40°-55°. Therefore, the angle of the surface wind across the front is determined by both the surface wind speed and propagation speed of gravity current.

One interesting implication can be obtained regarding the component of background wind perpendicular to the front U_{\perp} , which is generally a key factor in determining wave characteristics for orographic GWs. Since $U_{\perp} = U_{\rm surf} \times \sin \alpha = U_{\rm surf} \times \frac{c_{\rm gc}}{U_{\rm surf}} = c_{\rm gc}$ and $c_{\rm gc} = \sqrt{2g'H_{\rm gc}}$, U_{\perp} does not explicitly depend on the total background wind $U_{\rm surf}$. This implies that an increase in $U_{\rm surf}$ leads to a decrease in α , and consequently, the resultant

KOHMA ET AL. 14 of 22

21698996, 2024, 3, Downloaded from https://agupubs.onlinelibrary.wiley.com/doi/10.1029/2023JD039425, Wiley Online Library on [02/12/2024]. See the Terms and Conditions (https://onlinelibrary.wiley.com/terms

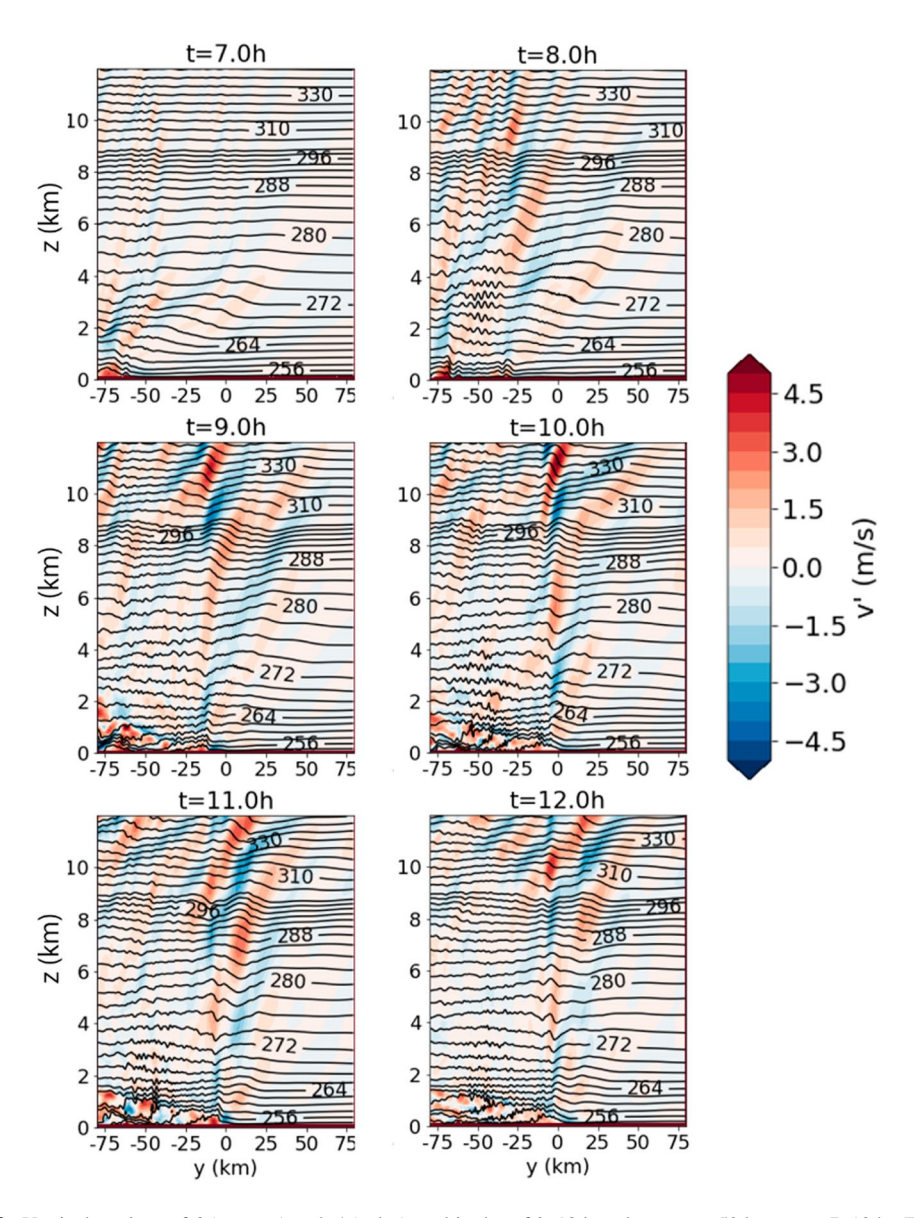


Figure 13. Vertical sections of θ (contour) and v' (color) at altitudes of 0–12 km along x = -50 km at t = 7-12 hr. The contour interval is 2 K (5 K) for $\theta = 250-300$ K (300–350 K).

 U_{\perp} does not change. Nonetheless, the total background wind $U_{\rm surf}$ plays a significant role in determining wave characteristics because the depth of the hydraulic jump occurring at the steep terrain of the continent, and thus depth of gravity current $H_{\rm sc}$, will depend on $U_{\rm surf}$.

In summary, the present simulation suggests the occurrence of GW radiation downwind of a hydraulic jump, which will be classified as a type of GW radiation processes resulting from the interaction between surface frontal structures and cross-front winds (Kilpatrick et al., 2014; Plougonven & Snyder, 2007; Ralph et al., 1999). As indicated in Figure 16, three-dimensional simulations, rather than two-dimensional simulations, are necessary to reproduce such a GW radiation process. The following remarks can be made about this GW radiation:

- Supercritical downslope flow (Froude number greater than 1) is in general associated with hydraulic jump occurrence. The steep topography and frequent occurrence of strong surface winds on the coast of Antarctica (Parish & Bromwich, 1987) make it a potential hot spot of this type of GW radiation while the shock-like structure along the coastal region has been reported in the midlatitudes (Burk & Thompson, 2004).
- The horizontal wavelength of the GWs is longer than that of small-scale (turbulent) disturbances and should depend on the horizontal scale of the isentropic surface hump.

KOHMA ET AL. 15 of 22

21698996, 2024, 3, Downloaded from https://agupubs.onlinelibrary.wiley.com/doi/10.1029/2023JD039425, Wiley Online Library on [02/12/2024]. See the Terms and Conditions (https://onlinelibrary.wiley.com/terms-and-conditions) on Wiley Online Library for rules of use; OA

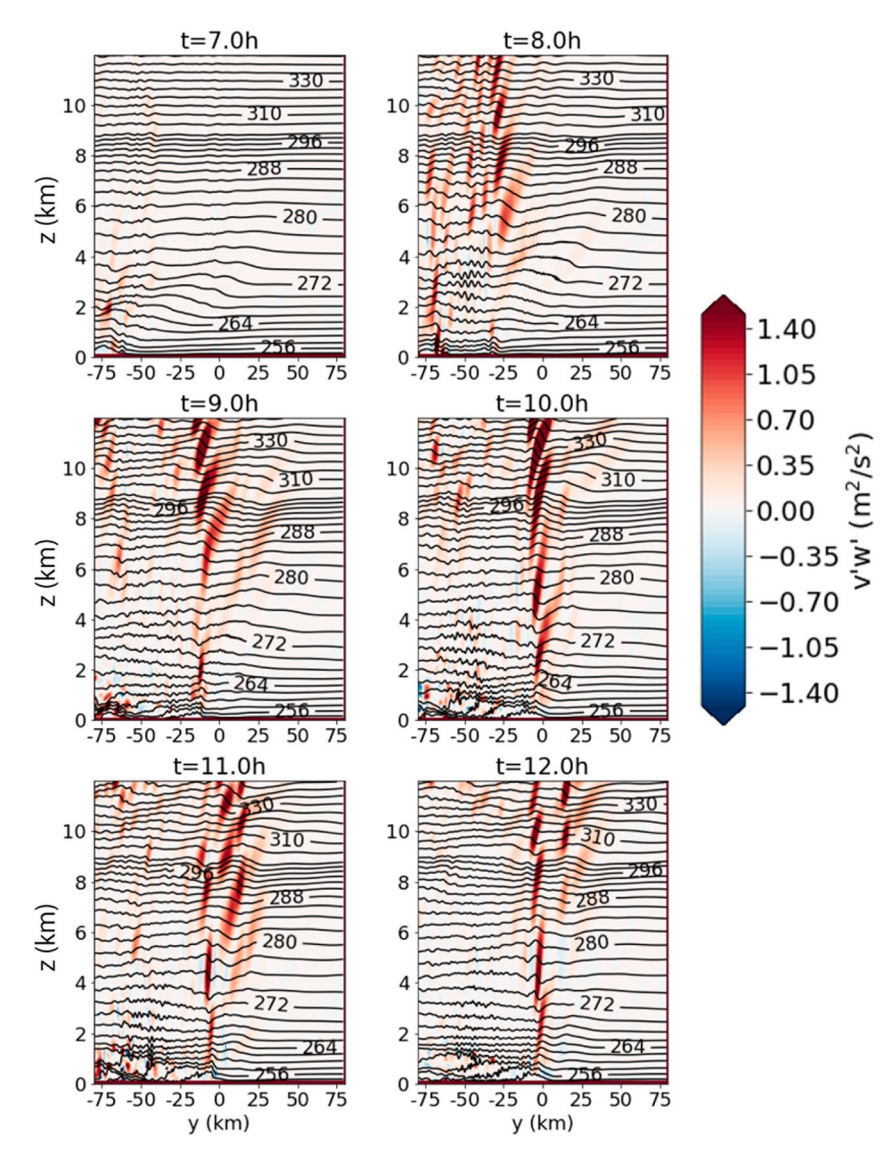


Figure 14. Same as Figure 13 but for θ (contour) and v'w' (color).

- The phase lines of the GWs are aligned with the isentropic surface hump near the surface, meaning that the horizontal wavenumber vector is not parallel to the coastal slope, as is typically observed for orographic GWs.
- Numerical models aiming to simulate the GW radiation downwind of a hydraulic jump should explicitly resolve small-scale (turbulent) eddies or use boundary-layer parameterizations to capture small-scale (turbulent) disturbances near the surface.

7. Concluding Remarks

A numerical simulation of GWs observed by a radar at Syowa Station, Antarctic on 18 May 2021 was conducted using a high-resolution model. The horizontal grid spacing is 250 m in the central domain and vertical grid spacing is 60 m, both of which are much higher than those used in the previous GW modeling studies over Syowa Station. The simulation successfully reproduced the observed features of the GWs, including the amplitude of vertical wind disturbances in the troposphere and vertical fluxes of northward momentum in the lower stratosphere. The modeling results include the following:

KOHMA ET AL. 16 of 22

21698996, 2024, 3, Downloaded from https://agupubs.onlinelibrary.wiley.com/doi/10.1029/2023JD039425, Wiley Online Library on [02/12/2024]. See the Terms and Conditions (https://onlinelibrary.wiley.com/te

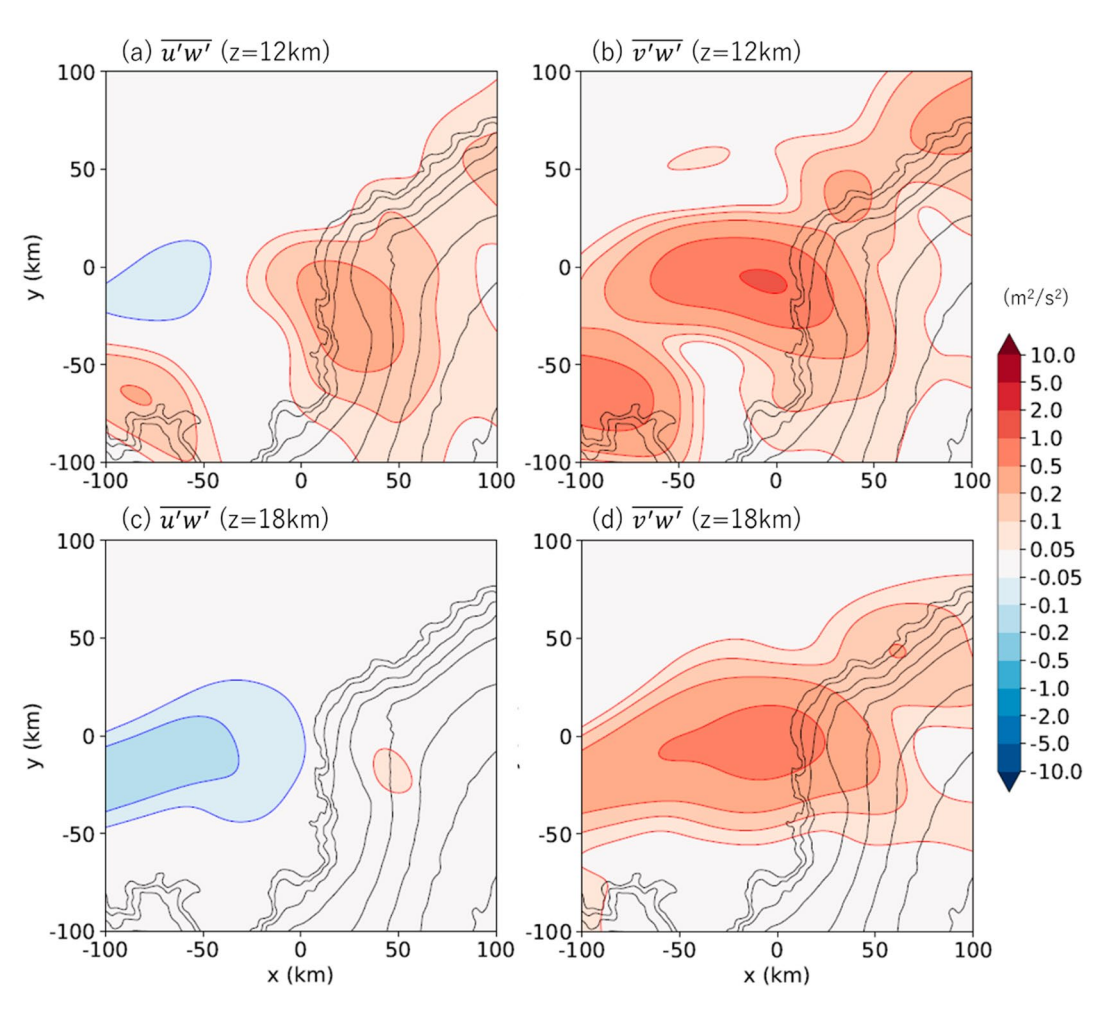


Figure 15. (a, b) Horizontal maps of (a) $\overline{u'w'}$ and (b) $\overline{v'w'}$ at an altitude of 12 km at t = 12 hr. Black contours indicate terrain elevation with an interval of 150 m. Colors are almost logarithmic scale. Panels (c, d) same as panels (a, b) but for an altitude of 18 km.

- In the troposphere, ship-wave responses are observed along the small coastal topography northeast of Syowa Station, while in the stratosphere, wave filtering in the directional vertical shear of background winds causes a significant change in the wave pattern.
- A multi-layer structure of small-scale turbulent vorticity was simulated over Syowa Station in the lower stratosphere as is consistent with radar observations, and the simulated volume rendering of vorticity shows horseshoe-shaped vortex tubes, indicative of GW breaking.
- The simulation shows another wave pattern with a horizontal wavelength of about 25 km is seen in the lower stratosphere west of Syowa Station, whose phase line is aligned with the turbulent wake front downwind of a hydraulic jump that occurs over the steep terrain.
- The observed GWs are likely radiated from the adiabatic lift of an airmass along the isentropic surface hump near the ground, which explains the northward momentum fluxes observed by the radar in the lower stratosphere.

The height variation of GW amplitude and phase correlates with background wind direction profile, as predicted by the linear theory (e.g., Shutts, 1998) and other numerical simulations (e.g., Eckermann et al., 2007; Guarino et al., 2018). Eckermann et al. (2007) examined changes in wave patterns with altitude as observed from space and concluded that it strongly related with the variation of background winds with height. While the present simulation shows a similar change in the wave pattern with altitude, it also reveals turbulent small-scale vortex tubes around the critical level, which are indicative of GW breaking. A comparison between high-resolution

KOHMA ET AL. 17 of 22

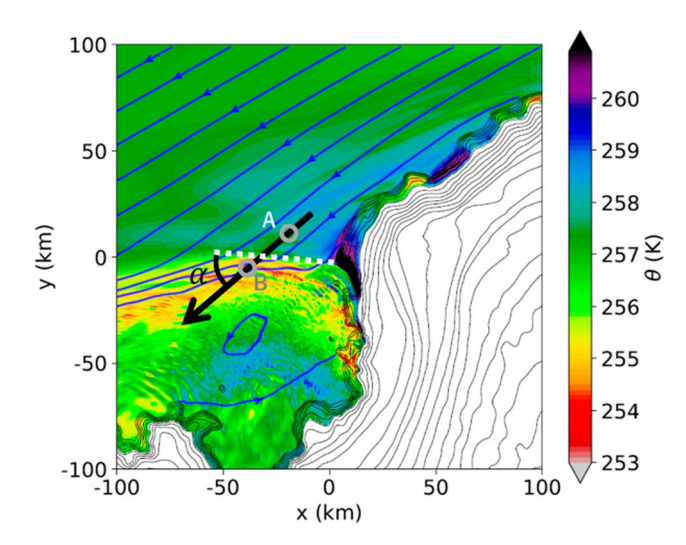


Figure 16. A horizontal map of θ (color) at an altitude of 0.5 km at t = 12 hr with the elevation of terrain (thin gray contours). The contour interval is 50 m. Blue curves with arrows indicate directions of surface winds at t = 12 hr. A broken white line indicates the isentropic surface hump. A black arrow indicates the direction of the surface wind leeward of gravity current. The points for the reference of upwind and downwind of the front is denoted by A and B (gray open circles), respectively.

simulations and vertical profiles of turbulent energy dissipation rates from the radar is promising for further case

Finally, although the present study focused on the MWs and their responses in the troposphere and lower stratosphere, the simulation covers from the troposphere to mesosphere, and we are currently analyzing GW dynamics in the upper stratosphere and mesosphere. We will report the results in the literature elsewhere.

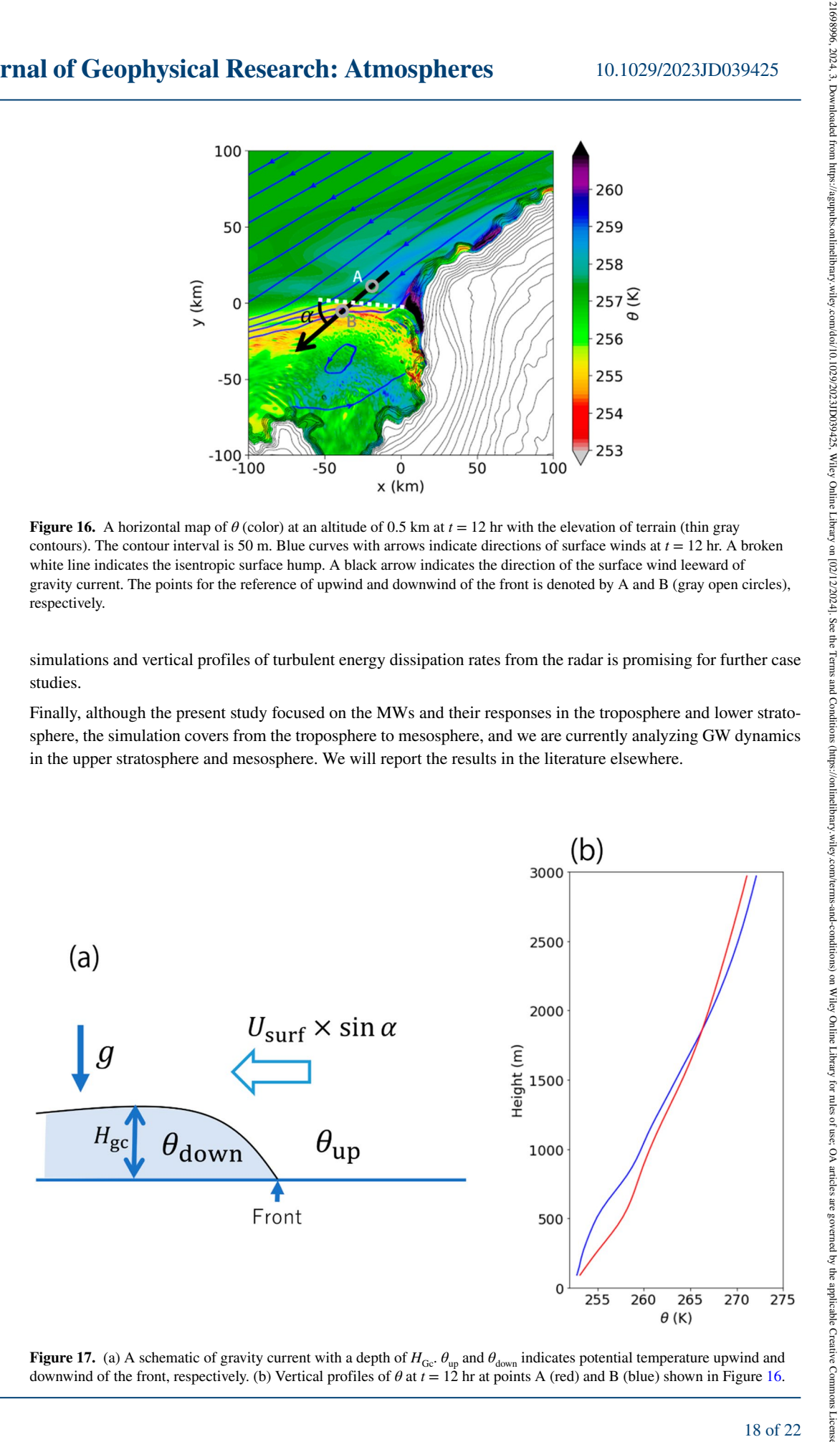


Figure 17. (a) A schematic of gravity current with a depth of H_{Gc} : θ_{up} and θ_{down} indicates potential temperature upwind and downwind of the front, respectively. (b) Vertical profiles of θ at t = 12 hr at points A (red) and B (blue) shown in Figure 16.

KOHMA ET AL. 18 of 22

21698996, 2024, 3, Downloaded from https://agupubs.onlinelibrary.wiley

.com/doi/10.1029/2023JD039425, Wiley Online Library on [02/12/2024]. See the Terms

Data Availability Statement

MERRA2 three-hourly data on pressure levels (Global Modeling and Assimilation Office, 2015) are available from the Goddard Earth Sciences Data and Information Services Center (https://doi.org/10.5067/QBZ6MG944HW0). ERA5 hourly data on pressure levels (Hersbach et al., 2023) are available from the Copernicus Climate Change Service Climate Data Store (https://doi.org/10.24381/cds.bd0915c6). RAMPv2 data are available from the NASA National Snow and Ice Data Center Distributed Active Archive Center (https://doi.org/10.5067/8JKNEW6B-FRVD). Other data that the present study and Supporting Information are available from https://doi.org/10.5281/zenodo.7998420.

Acknowledgments

The present study was supported by JST FOREST JPMJFR2231 and JSPS KAKENHI Grants 19K14791 and 22H00169. The Program of the Antarctic Syowa Mesosphere-Stratosphere-Troposphere/Incoherent Scatter (PANSY) radar is a multi-institutional project with core members from the University of Tokyo, the National Institute of Polar Research, and Kyoto University. The PANSY radar measurements at Syowa Station are performed by the Japanese Antarctic Research Expedition (JARE). This study is supported by the Cooperative Research Activities of Collaborative Use of Computing Facility of the Atmosphere and Ocean Research Institute, the University of Tokyo.

References

- Alexander, M. J., Geller, M., McLandress, C., Polavarapu, S., Preusse, P., Sassi, F., et al. (2010). Recent developments in gravity-wave effects in climate models and the global distribution of gravity-wave momentum flux from observations and models. *Quarterly Journal of the Royal Meteorological Society*, 136(650), 1103–1124. https://doi.org/10.1002/qj.637
- Alexander, M. J., & Teitelbaum, H. (2007). Observation and analysis of a large amplitude mountain wave event over the Antarctic Peninsula. Journal of Geophysical Research, 112(D21), D21103. https://doi.org/10.1029/2006jd008368
- Alexander, S. P., Klekociuk, A. R., McDonald, A. J., & Pitts, M. C. (2013). Quantifying the role of orographic gravity waves on polar stratospheric cloud occurrence in the Antarctic and the Arctic. *Journal of Geophysical Research-Atmospheres*, 118(20), 11493–11507. https://doi.org/10.1002/2013jd020122
- Alexander, S. P., Klekociuk, A. R., Pitts, M. C., McDonald, A. J., & Arevalo-Torres, A. (2011). The effect of orographic gravity waves on Antarctic polar stratospheric cloud occurrence and composition. *Journal of Geophysical Research*, 116(D6), D06109. https://doi. org/10.1029/2010jd015184
- Alexander, S. P., Orr, A., Webster, S., & Murphy, D. J. (2017). Observations and fine-scale-model simulations of gravity waves over Davis, East Antarctica (69°S, 78°E). *Journal of Geophysical Research-Atmospheres*, 122(14), 7355–7370. https://doi.org/10.1002/2017jd026615
- Andreassen, Ø., Hvidsten, P. Ø., Fritts, D. C., & Arendt, S. (1998). Vorticity dynamics in a breaking internal gravity wave. Part 1. Initial instability evolution. *Journal of Fluid Mechanics*, 367, 27–46. https://doi.org/10.1017/S0022112098001645
- Andrews, D. G., Holton, J. R., & Leovy, C. B. (1987). Middle atmosphere dynamics (p. 489). Academic Press.
- Arnault, J., & Kirkwood, S. (2012). Dynamical influence of gravity waves generated by the Vestfjella Mountains in Antarctica: Radar observations, fine-scale modelling and kinetic energy budget analysis. *Tellus Series A-Dynamic Meteorology and Oceanography*, 64(1), 17261. https://doi.org/10.3402/tellusa.v64i0.17261
- Benjamin, T. B. (1968). Gravity currents and related phenomena. Journal of Fluid Mechanics, 31(2), 209–248. https://doi.org/10.1017/S0022112068000133
- Bossert, K., Fritts, D. C., Pautet, P. D., Williams, B. P., Taylor, M. J., Kaifler, B., et al. (2015). Momentum flux estimates accompanying multiscale gravity waves over Mount Cook, New Zealand, on 13 July 2014 during the DEEPWAVE campaign. *Journal of Geophysical Research-Atmospheres*, 120(18), 9323–9337. https://doi.org/10.1002/2015jd023197
- Burk, S. D., & Thompson, W. T. (2004). Mesoscale eddy formation and shock features associated with a coastally trapped disturbance. *Monthly Weather Review*, 132(9), 2204–2223. https://doi.org/10.1175/1520-0493(2004)132<2204:Mefasf>2.0.Co;2
- Dong, W. J., Fritts, D. C., Thomas, G. E., & Lund, T. S. (2021). Modeling responses of polar mesospheric clouds to gravity wave and instability dynamics and induced large-scale motions. *Journal of Geophysical Research-Atmospheres*, 126(13), e2021JD034643. https://doi.org/10.1029/2021JD034643
- Durran, D. R. (1986). Another look at downslope windstorms. 1. The development of analogs to supercritical-flow in an infinitely deep, continuously stratified fluid. *Journal of the Atmospheric Sciences*, 43(21), 2527–2543. https://doi.org/10.1175/1520-0469(1986)043<2527: Aladwo>2.0.Co:2
- Durran, D. R. (1990). Mountain waves and downslope winds. In W. Blumen (Ed.), Atmospheric processes over complex terrain. Meteorological monographs (Vol. 23, pp. 59–81). https://doi.org/10.1007/978-1-935704-25-6_4
- Eckermann, S. D., Ma, J., Wu, D. L., & Broutman, D. (2007). A three-dimensional mountain wave imaged in satellite radiance throughout the stratosphere: Evidence of the effects of directional wind shear. *Quarterly Journal of the Royal Meteorological Society*, 133(629), 1959–1975. https://doi.org/10.1002/qj.187
- Fovell, R., Durran, D., & Holton, J. R. (1992). Numerical simulations of convectively generated stratospheric gravity waves. *Journal of the Atmospheric Sciences*, 49(16), 1427–1442. https://doi.org/10.1175/1520-0469(1992)049<1427:NSOCGS>2.0.CO;2
- Fritts, D. C., & Alexander, M. J. (2003). Gravity wave dynamics and effects in the middle atmosphere. Reviews of Geophysics, 41(1), 1003. https://doi.org/10.1029/2001rg000106
- Fritts, D. C., Arendt, S., & Andreassen, Ø. (1998). Vorticity dynamics in a breaking internal gravity wave. Part 2. Vortex interactions and transition to turbulence. *Journal of Fluid Mechanics*, 367, 47–65. https://doi.org/10.1017/S0022112098001633
- Fritts, D. C., Lund, A. C., Lund, T. S., & Yudin, V. (2022a). Impacts of limited model resolution on the representation of mountain wave and secondary gravity wave dynamics in local and global models. 1: Mountain waves in the stratosphere and mesosphere. *Journal of Geophysical Research-Atmospheres*, 127(9), e2021JD035990. https://doi.org/10.1029/2021JD035990
- Fritts, D. C., Lund, A. C., Lund, T. S., & Yudin, V. (2022b). Impacts of limited model resolution on the representation of mountain wave and secondary wave dynamics in local and global models: 2. Mountain wave and secondary wave evolutions in the thermosphere. *Journal of Geophysical Research-Atmospheres*, 127(9), e2021JD036035. https://doi.org/10.1029/2021JD036035
- Fritts, D. C., Lund, T. S., Wan, K., & Liu, H. L. (2021). Numerical simulation of mountain waves over the Southern Andes. Part II: Momentum fluxes and wave-mean-flow interactions. *Journal of the Atmospheric Sciences*, 78(10), 3069–3088. https://doi.org/10.1175/Jas-D-20-0207.1
- Fritts, D. C., Smith, R. B., Taylor, M. J., Doyle, J. D., Eckermann, S. D., Dörnbrack, A., et al. (2016). The deep propagating gravity wave experiment (DEEPWAVE): An airborne and ground-based exploration of gravity wave propagation and effects from their sources throughout the lower and middle atmosphere. *Bulletin of the American Meteorological Society*, 97(3), 425–453. https://doi.org/10.1175/Bams-D-14-00269.1
- Fritts, D. C., Vosper, S. B., Williams, B. P., Bossert, K., Plane, J. M. C., Taylor, M. J., et al. (2018). Large-amplitude mountain waves in the mesosphere accompanying weak cross-mountain flow during DEEPWAVE Research flight RF22. *Journal of Geophysical Research-Atmospheres*, 123(18), 9992–10022. https://doi.org/10.1029/2017jd028250

KOHMA ET AL. 19 of 22

21698996, 2024, 3, Downloaded from https://agupubs.onlinelibrary.wiley

com/doi/10.1029/2023JD039425,

- Fritts, D. C., Wang, L., Werne, J., Lund, T., & Wan, K. (2009). Gravity wave instability dynamics at high Reynolds numbers. Part II: Turbulence evolution, structure, and anisotropy. *Journal of the Atmospheric Sciences*, 66(5), 1149–1171. https://doi.org/10.1175/2008jas2727.1
- Fukao, S., Hamazu, K., & Doviak, R. J. (2014). Radar for meteorological and atmospheric observations. Springer. https://doi. org/10.1007/978-4-431-54334-3
- Gelaro, R., McCarty, W., Suarez, M. J., Todling, R., Molod, A., Takacs, L., et al. (2017). The Modern-Era Retrospective analysis for research and applications, version 2 (MERRA-2). *Journal of Climate*, 30(14), 5419–5454. https://doi.org/10.1175/Jcli-D-16-0758.1
- Germano, M., Piomelli, U., Moin, P., & Cabot, W. H. (1991). A dynamic subgrid-scale eddy viscosity model. *Physics of Fluids A: Fluid Dynamics*, 3(7), 1760–1765. https://doi.org/10.1063/1.857955
- Global Modeling and Assimilation Office (GMAO). (2015). inst3_3d_asm_Np: 3d, 3-hourly, instantaneous, pressure-level, assimilation, assimilated meteorological fields, version 5.12.4, Greenbelt, MD, USA [Dataset]. Goddard Earth Sciences Data and Information Services Center (GES DISC), https://doi.org/10.5067/OBZ6MG944HW0
- Grimsdell, A. W., Alexander, M. J., May, P. T., & Hoffmann, L. (2010). Model study of waves generated by convection with direct validation via satellite. *Journal of the Atmospheric Sciences*, 67(5), 1617–1631. https://doi.org/10.1175/2009jas3197.1
- Guarino, M. V., Teixeira, M. A. C., Keller, T. L., & Sharman, R. D. (2018). Mountain-wave turbulence in the presence of directional wind shear over the rocky Mountains. *Journal of the Atmospheric Sciences*, 75(4), 1285–1305. https://doi.org/10.1175/Jas-D-17-0128.1
- Hersbach, H., Bell, B., Berrisford, P., Biavati, G., Horányi, A., Muñoz Sabater, J., et al. (2023). ERA5 hourly data on pressure levels from 1940 to present [Dataset]. Copernicus Climate Change Service (C3S) Climate Data Store (CDS). https://doi.org/10.24381/cds.bd0915c6
- Hersbach, H., Bell, B., Berrisford, P., Hirahara, S., Horanyi, A., Munoz-Sabater, J., et al. (2020). The ERA5 global reanalysis. *Quarterly Journal of the Royal Meteorological Society*, 146(730), 1999–2049. https://doi.org/10.1002/qj.3803
- Hertzog, A., Boccara, G., Vincent, R. A., Vial, F., & Cocquerez, P. (2008). Estimation of gravity wave momentum flux and phase speeds from quasi-Lagrangian stratospheric balloon flights. Part II: Results from the Vorcore campaign in Antarctica. *Journal of the Atmospheric Sciences*, 65(10), 3056–3070. https://doi.org/10.1175/2008jas2710.1
- Hindley, N. P., Wright, C. J., Smitha, N. D., Hoffmann, L., Holt, L. A., Alexander, M. J., et al. (2019). Gravity waves in the winter stratosphere over the southern ocean: High-resolution satellite observations and 3-D spectral analysis. *Atmospheric Chemistry and Physics*, 19(24), 15377–15414. https://doi.org/10.5194/acp-19-15377-2019
- Hocking, W. K. (1983). On the extraction of atmospheric turbulence parameters from radar backscatter Doppler spectra—I. Theory. *Journal of Atmospheric and Terrestrial Physics*, 45(2–3), 89–102. https://doi.org/10.1016/s0021-9169(83)80013-0
- Hocking, W. K. (1985). Measurement of turbulent energy-dissipation rates in the middle atmosphere by radar techniques—A review. *Radio Science*, 20(6), 1403–1422. https://doi.org/10.1029/rs020i006p01403
- Hocking, W. K. (1999). The dynamical parameters of turbulence theory as they apply to middle atmosphere studies. *Earth Planets and Space*, 51(7–8), 525–541. https://doi.org/10.1186/Bf03353213
- Hoskins, B. J., McIntyre, M. E., & Robertson, A. W. (1985). On the use and significance of isentropic potential vorticity maps. *Quarterly Journal of the Royal Meteorological Society*, 111(470), 877–946. https://doi.org/10.1256/Smsqj.47001
- Jewtoukoff, V., Hertzog, A., Plougonven, R., de la Cámara, A., & Lott, F. (2015). Comparison of gravity waves in the southern hemisphere derived from balloon observations and the ECMWF analyses. *Journal of the Atmospheric Sciences*, 72(9), 3449–3468. https://doi.org/10.1175/ Jas-D-14-0324.1
- Kaifler, B., Lübken, F. J., Höffner, J., Morris, R. J., & Viehl, T. P. (2015). Lidar observations of gravity wave activity in the middle atmosphere over Davis (69°S, 78°E), Antarctica. *Journal of Geophysical Research-Atmospheres*, 120(10), 4506–4521. https://doi.org/10.1002/2014jd022879
- Kilpatrick, T., Schneider, N., & Qiu, B. (2014). Boundary layer convergence induced by strong winds across a midlatitude SST front. *Journal of Climate*, 27(4), 1698–1718. https://doi.org/10.1175/Jcli-D-13-00101.1
- Kim, Y. J., Eckermann, S. D., & Chun, H. Y. (2003). An overview of the past, present and future of gravity-wave drag parametrization for numerical climate and weather prediction models. Atmosphere-Ocean, 41(1), 65–98. https://doi.org/10.3137/ao.410105
- Kogure, M., Nakamura, T., Ejiri, M. K., Nishiyama, T., Tomikawa, Y., Tsutsumi, M., et al. (2017). Rayleigh/Raman lidar observations of gravity wave activity from 15 to 70 km altitude over Syowa (69 degrees S, 40 degrees E), the Antarctic. *Journal of Geophysical Research-Atmospheres*, 122(15), 7869–7880. https://doi.org/10.1002/2016jd026360
- Kohma, M., & Sato, K. (2011). The effects of atmospheric waves on the amounts of polar stratospheric clouds. Atmospheric Chemistry and Physics, 11(22), 11535–11552. https://doi.org/10.5194/acp-11-11535-2011
- Kohma, M., Sato, K., Nishimura, K., & Tsutsumi, M. (2021). Weakening of polar mesosphere winter echo and turbulent energy dissipation rates after a stratospheric sudden warming in the southern hemisphere in 2019. Geophysical Research Letters, 48(10), e2021GL092705. https://doi. org/10.1029/2021GL092705
- Kohma, M., Sato, K., Tomikawa, Y., Nishimura, K., & Sato, T. (2019). Estimate of turbulent energy dissipation rate from the VHF radar and radio-sonde observations in the Antarctic. *Journal of Geophysical Research-Atmospheres*, 124(6), 2976–2993. https://doi.org/10.1029/2018jd029521
- Koshin, D., Sato, K., Kohma, M., & Watanabe, S. (2022). An update on the 4D-LETKF data assimilation system for the whole neutral atmosphere. Geoscientific Model Development, 15(5), 2293–2307. https://doi.org/10.5194/gmd-15-2293-2022
- Koshin, D., Sato, K., Miyazaki, K., & Watanabe, S. (2020). An ensemble Kalman filter data assimilation system for the whole neutral atmosphere. Geoscientific Model Development, 13(7), 3145–3177. https://doi.org/10.5194/gmd-13-3145-2020
- Kruse, C. G., Alexander, M. J., Hoffmann, L., van Niekerk, A., Polichtchouk, I., Bacmeister, J. T., et al. (2022). Observed and modeled mountain waves from the surface to the mesosphere near the Drake passage. *Journal of the Atmospheric Sciences*, 79(4), 909–932. https://doi.org/10.1175/Jas-D-21-0252.1
- Kuettner, J. P., Hildebrand, P. A., & Clark, T. L. (1987). Convection waves—Observations of gravity-wave systems over convectively active boundary-layers. Quarterly Journal of the Royal Meteorological Society, 113(476), 445–467. https://doi.org/10.1256/smsqj.47602
- Landau, L. D., & Lifshitz, E. M. (1987). Chapter IX—SHOCK WAVES. In L. D. Landau & E. M. Lifshitz (Eds.), Fluid mechanics (2nd ed., pp. 313–360). Pergamon. https://doi.org/10.1016/B978-0-08-033933-7.50017-9
- Li, Z., Robinson, W., & Liu, A. Z. (2009). Sources of gravity waves in the lower stratosphere above South Pole. *Journal of Geophysical Research*, 114(D14), D14103. https://doi.org/10.1029/2008jd011478
- Liu, H., Jezek, K. C., Li, B., & Zhao, Z. (2015). Radarsat Antarctic mapping project digital elevation model, version 2. Boulder, Colorado USA [Dataset]. NASA National Snow and Ice Data Center Distributed Active Archive Center (NSIDC DAAC). https://doi.org/10.5067/8JKNEW6BFRVD
- Lund, T. S., Fritts, D. C., Wan, K., Laughman, B., & Liu, H. L. (2020). Numerical simulation of mountain waves over the southern Andes. Part I: Mountain wave and secondary wave character, evolutions, and breaking. *Journal of the Atmospheric Sciences*, 77(12), 4337–4356. https://doi.org/10.1175/Jas-D-19-0356.1

KOHMA ET AL. 20 of 22

21698996, 2024, 3, Downloaded from https

.com/doi/10.1029/2023JD039425, Wiley Online Library on

- McLandress, C., Shepherd, T. G., Polavarapu, S., & Beagley, S. R. (2012). Is missing orographic gravity wave drag near 60 degrees S the cause of the stratospheric zonal wind biases in chemistry climate models? *Journal of the Atmospheric Sciences*, 69(3), 802–818. https://doi.org/10.1175/Jas-D-11-0159.1
- Minamihara, Y., Sato, K., & Tsutsumi, M. (2020). Intermittency of gravity waves in the Antarctic troposphere and lower stratosphere revealed by the PANSY radar observation. *Journal of Geophysical Research-Atmospheres*, 125(15), e2020JD032543. https://doi.org/10.1029/2020JD032543
- Minamihara, Y., Sato, K., & Tsutsumi, M. (2023). Kelvin-helmholtz billows in the troposphere and lower stratosphere detected by the PANSY radar at Syowa station in the Antarctic. *Journal of Geophysical Research: Atmospheres*, 128(5), e2022JD036866. https://doi.org/10.1029/2022JD036866
- Minamihara, Y., Sato, K., Tsutsumi, M., & Sato, T. (2018). Statistical characteristics of gravity waves with near-inertial frequencies in the Antarctic troposphere and lower stratosphere observed by the PANSY radar. *Journal of Geophysical Research-Atmospheres*, 123(17), 8993–9010. https://doi.org/10.1029/2017jd028128
- Moin, P., Squires, K., Cabot, W., & Lee, S. (1991). A dynamic subgrid-scale model for compressible turbulence and scalar transport. Physics of Fluids A: Fluid Dynamics. 3(11), 2746–2757. https://doi.org/10.1063/1.858164
- Murphy, D. J., Alexander, S. P., Klekociuk, A. R., Love, P. T., & Vincent, R. A. (2014). Radiosonde observations of gravity waves in the lower stratosphere over Davis, Antarctica. *Journal of Geophysical Research-Atmospheres*, 119(21), 11973–11996. https://doi.org/10.1002/2014jd022448
- Nishimura, K., Kohma, M., Sato, K., & Sato, T. (2020). Spectral observation theory and beam debroadening algorithm for atmospheric radar. *IEEE Transactions on Geoscience and Remote Sensing*, 58(10), 6767–6775. https://doi.org/10.1109/Tgrs.2020.2970200
- Noel, V., & Pitts, M. (2012). Gravity wave events from mesoscale simulations, compared to polar stratospheric clouds observed from spaceborne lidar over the Antarctic Peninsula. *Journal of Geophysical Research*, 117(D11), D11207. https://doi.org/10.1029/2011jd017318
- O'Sullivan, D., & Dunkerton, T. J. (1995). Generation of inertia–gravity waves in a simulated life cycle of baroclinic instability. *Journal of the Atmospheric Sciences*, 52(21), 3695–3716. https://doi.org/10.1175/1520-0469(1995)052<3695:GOIWIA>2.0.CO;2
- Parish, T. R., & Bromwich, D. H. (1987). The surface windfield over the Antarctic Ice Sheets. *Nature*, 328(6125), 51–54. https://doi.
- org/10.1038/328051a0
 Pfenninger, M., Liu, A. Z., Papen, G. C., & Gardner, C. S. (1999). Gravity wave characteristics in the lower atmosphere at south pole. *Journal of*
- Geophysical Research, 104(D6), 5963–5984. https://doi.org/10.1029/98jd02705

 Plougonven, R., Hertzog, A., & Guez, L. (2013). Gravity waves over Antarctica and the southern ocean: Consistent momentum fluxes in mesos-
- Plougonven, R., Hertzog, A., & Guez, L. (2013). Gravity waves over Antarctica and the southern ocean: Consistent momentum fluxes in mesoscale simulations and stratospheric balloon observations. Quarterly Journal of the Royal Meteorological Society, 139(670), 101–118. https://doi.org/10.1002/qj.1965
- Plougonven, R., & Snyder, C. (2007). Inertia–gravity waves spontaneously generated by jets and fronts. Part I: Different Baroclinic Life cycles. Journal of the Atmospheric Sciences, 64(7), 2502–2520. https://doi.org/10.1175/JAS3953.1
- Plougonven, R., & Zhang, F. Q. (2014). Internal gravity waves from atmospheric jets and fronts. Reviews of Geophysics, 52(1), 33–76. https://doi.org/10.1002/2012rg000419
- Ralph, F. M., Mazaudier, C., Crochet, M., & Venkateswaran, S. V. (1993). Doppler Sodar and radar wind-profiler observations of gravity-wave activity associated with a gravity current. *Monthly Weather Review*, 121(2), 444–463. https://doi.org/10.1175/1520-0493(1993)121<0444:Dsarwp>2.0.Co;2
- Ralph, F. M., Neiman, P. J., & Keller, T. L. (1999). Deep-tropospheric gravity waves created by leeside cold fronts. *Journal of the Atmospheric Sciences*, 56(17), 2986–3009. https://doi.org/10.1175/1520-0469(1999)056<2986:Dtgwcb>2.0.Co;2
- Rottman, J. W., & Simpson, J. E. (1989). The Formation of internal bores in the atmosphere—A laboratory model. *Quarterly Journal of the Royal Meteorological Society*, 115(488), 941–963. https://doi.org/10.1256/smsqi.48808
- Sato, K., Kohma, M., Tsutsumi, M., & Sato, T. (2017). Frequency spectra and vertical profiles of wind fluctuations in the summer Antarctic mesosphere revealed by MST radar observations. *Journal of Geophysical Research-Atmospheres*, 122(1), 3–19. https://doi.org/10.1002/2016id025834
- Sato, K., O'Sullivan, D. J., & Dunkerton, T. J. (1997). Low-frequency inertia-gravity waves in the stratosphere revealed by three-week continuous observation with the MU radar. *Geophysical Research Letters*, 24(14), 1739–1742. https://doi.org/10.1029/97gl01759
- Sato, K., Tateno, S., Watanabe, S., & Kawatani, Y. (2012). Gravity wave characteristics in the southern hemisphere revealed by a high-resolution middle-atmosphere general circulation model. *Journal of the Atmospheric Sciences*, 69(4), 1378–1396. https://doi.org/10.1175/Jas-D-11-0101.1
- Sato, K., Tsutsumi, M., Sato, T., Nakamura, T., Saito, A., Tomikawa, Y., et al. (2014). Program of the Antarctic Syowa MST/IS radar (PANSY). Journal of Atmospheric and Solar-Terrestrial Physics, 118, 2–15. https://doi.org/10.1016/j.jastp.2013.08.022
- Sato, K., Watanabe, S., Kawatani, Y., Tomikawa, Y., Miyazaki, K., & Takahashi, M. (2009). On the origins of mesospheric gravity waves. Geophysical Research Letters, 36(19), L19801. https://doi.org/10.1029/2009gl039908
- Sato, K., & Yoshiki, M. (2008). Gravity wave generation around the polar vortex in the stratosphere revealed by 3-hourly radiosonde observations at Syowa station. *Journal of the Atmospheric Sciences*, 65(12), 3719–3735. https://doi.org/10.1175/2008jas2539.1
- Shibuya, R., Sato, K., Tsutsumi, M., Sato, T., Tomikawa, Y., Nishimura, K., & Kohma, M. (2017). Quasi-12 h inertia-gravity waves in the lower mesosphere observed by the PANSY radar at Syowa Station (39.6 degrees E, 69.0 degrees S). Atmospheric Chemistry and Physics, 17(10), 6455–6476. https://doi.org/10.5194/acp-17-6455-2017
- Shutts, G. J. (1998). Stationary gravity-wave structure in flows with directional wind shear. Quarterly Journal of the Royal Meteorological Society, 124(549), 1421–1442. https://doi.org/10.1002/qj.49712454905
- Smith, R. B. (2019). 100 years of progress on mountain meteorology research. Meteorological Monographs, 59, 20.21–20.73. https://doi.org/10.1175/AMSMONOGRAPHS-D-18-0022.1
- Smith, S. M., Vadas, S. L., Baggaley, W. J., Hernandez, G., & Baumgardner, J. (2013). Gravity wave coupling between the mesosphere and thermosphere over New Zealand. *Journal of Geophysical Research-Space Physics*, 118(5), 2694–2707. https://doi.org/10.1002/jgra.50263
- Tsuda, T., Sato, T., Hirose, K., Fukao, S., & Kato, S. (1986). MU radar observations of the aspect sensitivity of backscattered Vhf Echo power in the troposphere and lower stratosphere. *Radio Science*, 21(6), 971–980. https://doi.org/10.1029/RS021i006p00971
- Vadas, S. L., & Becker, E. (2018). Numerical modeling of the excitation, propagation, and dissipation of primary and secondary gravity waves during Wintertime at McMurdo station in the Antarctic. *Journal of Geophysical Research-Atmospheres*, 123(17), 9326–9369. https://doi. org/10.1029/2017jd027974
- Vignon, É., Picard, G., Durán-Alarcón, C., Alexander, S. P., Gallée, H., & Berne, A. (2020). Gravity wave excitation during the coastal transition of an extreme katabatic flow in Antarctica. *Journal of the Atmospheric Sciences*. 77(4), 1295–1312. https://doi.org/10.1175/Jas-D-19-0264.1
- Vincent, R. A., & Reid, I. M. (1983). HF Doppler measurements of mesospheric gravity-wave momentum fluxes. *Journal of the Atmospheric Sciences*, 40(5), 1321–1333. https://doi.org/10.1175/1520-0469(1983)040<1321:Hdmomg>2.0.Co;2
- Vosper, S. B. (2015). Mountain waves and wakes generated by south Georgia: Implications for drag parametrization. Quarterly Journal of the Royal Meteorological Society, 141(692), 2813–2827. https://doi.org/10.1002/qj.2566

KOHMA ET AL. 21 of 22



Journal of Geophysical Research: Atmospheres

- 10.1029/2023JD039425
- Vosper, S. B., Brown, A. R., & Webster, S. (2016). Orographic drag on islands in the NWP mountain grey zone. *Quarterly Journal of the Royal Meteorological Society*, 142(701), 3128–3137. https://doi.org/10.1002/qj.2894
- Watanabe, S., Sato, K., & Takahashi, M. (2006). A general circulation model study of the orographic gravity waves over Antarctica excited by katabatic winds. *Journal of Geophysical Research*, 111(D18), D18104. https://doi.org/10.1029/2005jd006851
- Weinstock, J. (1981). Using radar to estimate dissipation rates in thin-layers of turbulence. *Radio Science*, 16(6), 1401–1406. https://doi.org/10.1029/RS016i006p01401
- Wilson, R. (2004). Turbulent diffusivity in the free atmosphere inferred from MST radar measurements: A review. *Annales Geophysicae*, 22(11), 3869–3887. https://doi.org/10.5194/angeo-22-3869-2004
- Wright, C. J., Hindley, N. P., Hoffmann, L., Alexander, M. J., & Mitchell, N. J. (2017). Exploring gravity wave characteristics in 3-D using a novel S-transform technique: AIRS/Aqua measurements over the southern Andes and Drake passage. *Atmospheric Chemistry and Physics*, 17(13), 8553–8575. https://doi.org/10.5194/acp-17-8553-2017
- Yamashita, C., Chu, X. Z., Liu, H. L., Espy, P. J., Nott, G. J., & Huang, W. T. (2009). Stratospheric gravity wave characteristics and seasonal variations observed by lidar at the South Pole and Rothera, Antarctica. *Journal of Geophysical Research*, 114(D12), D12101. https://doi.org/10.1029/2008jd011472
- Yasuda, Y., Sato, K., & Sugimoto, N. (2015). A theoretical study on the spontaneous radiation of inertia-gravity waves using the renormalization group method. Part II: Verification of the theoretical equations by numerical simulation. *Journal of the Atmospheric Sciences*, 72(3), 984–1009. https://doi.org/10.1175/Jas-D-13-0371.1
- Yoo, J. H., Choi, T., Chun, H. Y., Kim, Y. H., Song, I. S., & Song, B. G. (2018). Inertia-gravity waves revealed in radiosonde data at Jang Bogo station, Antarctica (74 degrees 37'S, 164 degrees 13'E): 1. Characteristics, energy, and momentum flux. *Journal of Geophysical Research-Atmospheres*, 123(23), 13305–13331. https://doi.org/10.1029/2018jd029164
- Yoshiki, M., & Sato, K. (2000). A statistical study of gravity waves in the polar regions based on operational radiosonde data. *Journal of Geophysical Research*, 105(D14), 17995–18011. https://doi.org/10.1029/2000jd900204

KOHMA ET AL. 22 of 22